2015

Modeling Phase Change Heat Transfer of Liquid/vapor Systems in Free/porous Media

James Wilson
University of Central Florida

STARS Citation

Wilson, James, "Modeling Phase Change Heat Transfer of Liquid/vapor Systems in Free/porous Media" (2015). *Electronic Theses and Dissertations, 2004-2019*. 1476.
https://stars.library.ucf.edu/etd/1476

MODELING PHASE CHANGE HEAT TRANSFER OF LIQUID/VAPOR SYSTEMS IN FREE AND POROUS MEDIA

by

JAMES WILSON
B.S. University of Central Florida, 2013

A thesis submitted in partial fulfillment of the requirements
for the degree of Master of Science in Mechanical Engineering
in the Department of Mechanical and Aerospace Engineering
in the College of Engineering and Computer Science
at the University of Central Florida
Orlando, Florida

Fall Term
2015

ABSTRACT

Effective solvent extraction incorporating electromagnetic heating is a relatively new concept that relies on Radio Frequency heating and solvents to replace steam in current thermal processes for the purpose of extracting bitumen from oil rich sands. The work presented here will further the understanding of the near wellbore flow of this two phase system in order to better predict solvent vaporization dynamics and heat rates delivered to the pay zone. This numerical study details the aspects of phase change of immiscible, two component, liquid/vapor systems confined in porous media heated by electromagnetic radiation, approximated by a spatially dependent volumetric heat source term in the energy equation. The objective of this work is to utilize the numerical methodology presented herein to predict maximum solvent delivery rates to a heated isotropic porous matrix to avoid the over-saturation of the heated pay zone. The total liquid mass content and mean temperature in the domain are monitored to assess whether the liquid phase is fully vaporized prior to flowing across the numerical domain boundary. The distribution of the volumetric heat generation rate used to emulate the physics of electromagnetic heating in the domain decays away from the well bore. Some of the heat generated acts to superheat the already vaporized solvent away from the interface, requiring heat delivery rates that are many times greater than the energy required to turn the liquid solvent to vapor determined by an energy balance. Results of the parametric study from the pay zone simulations demonstrate the importance of the Darcian flow resistance forces added by the porous media to stabilize the flow being pulled away from the wellbore in the presence of gravity. For all cases involving an increase in solvent delivery rate with a constant heat rate, the permeability range required for full vaporization must decrease in order to balance the gravitational forces pulling the solvent from the heated region. For all conditions of permeability and solvent delivery rates, sufficiently increasing the heat rate results in complete vaporization of the liquid solvent. For the case of decreasing solvent delivery rate, a wider range of higher permeabilities for a given heat rate can be utilized while achieving full vaporization. A three dimensional surface outlining the transition from partially vaporized to fully vaporized regimes is constructed relating the solvent delivery rate, the permeability of the porous near wellbore zone and the heat rate supplied to the domain. For the range of permeabilities ($\approx 3000mD$) observed in these types of well bores, low solvent delivery rates and high heat rates must be utilized in order to achieve full vaporization.

This thesis is dedicated to Dr. Jonathan D. Wehking for our friendship, for his dedication to fostering a collaborative work environment and for pushing me to pursue personal and professional betterment. A large part of my personal, professional and technical skill development is owed to him. To Dr. Kumar for providing me with the means to work in this environment and continually advocating for me as professional role model. To my family for their love and support and for their understanding of my responsibilities as a student.

ACKNOWLEDGMENTS

A portion of this work is credited to Paul Wiegand and the dedicated staff that maintain STOKES, the High Performance Computing cluster at The University of Central Florida's Advanced Research Computing Center. A special thanks is also given to Mark Blue and Mark Trautman at Harris for the continued technical support and funding to conduct this research.

TABLE OF CONTENTS

LIST OF FIGURES

LIST OF TABLES

CHAPTER 1: INTRODUCTION

Technological advancements in the field of petroleum engineering have paved the way for extracting and processing oil in cost effective and innovative ways. For the last few decades, Steam Assisted Gravity Drainage (SAGD) and other such technologies have allowed for the extraction of oil from reservoirs that had previously been uneconomical. In most cases, these bitumen rich oil sands are nearly solid formations that require the addition of heat to mobilize the oil. SAGD involves drilling two well bores horizontally into a bitumen rich reservoir. The upper bore (injector) carries pressurized steam to the pay zone, heating and mobilizing the bitumen. As gravity works to drain the decreased viscosity oil, the second well, drilled below the injector, produces the oil to the surface for processing. Electromagnetic heating relies fundamentally on the same principles, however, the use of steam is replaced by a combined effect of Radio Frequency (RF) energy and solvents such as propane and butane. The RF energy preheats the bitumen to a moderate temperature which lowers the bitumen viscosity and accelerates diffusion of the solvent into the bitumen. The bitumen viscosity is further reduced by the dilution of the solvent.

In a review of current electromagnetic heating technology, numerous numerical and experimental studies have demonstrated the potential viability of these technologies, most of which are still in their infant stages [1, 2]. In the current study, OpenFOAM was utilized to build the phase change solver and also include the necessary modifications to the momentum and Volume of Fluid (VOF) equations to account for the presence of porous media. The flow model utilizes a Darcy-Brinkman [3, 4, 5] form of Navier-Stokes equations coupled with the VOF equation to track the progression of a sharp interface through the oil sand. The phase change model relies on a smeared source term distribution developed by Hardt and Wondra [6] with modifications proposed by Kunklemann [7] to redistribute source terms away from the transition region at the sharp liquid/vapor interface.

This work aims to further the understanding of near wellbore flow for the case of immiscible two phase flow of liquid/vapor propane through free and porous media undergoing electro magnetic heating by RF energy. The domain of interest is confined to the injector well bore (Fig.1.1) where the inflow of solvent is liquid at the saturation temperature for the given pressure. The solvent flow is distributed uniformly about the periphery of the solvent delivery pipe and permeates into the porous media initially at the saturation temperature in the presence of gravity.

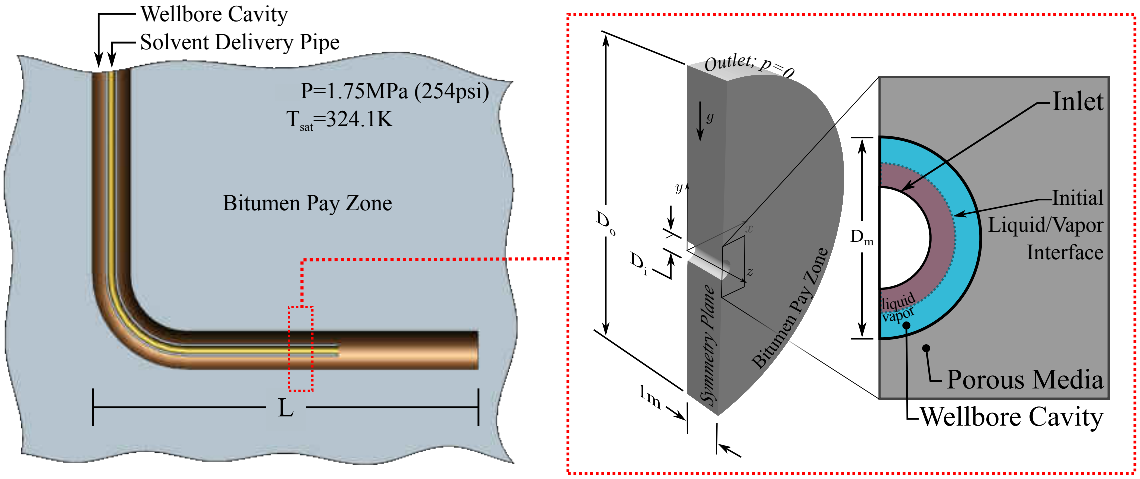

Figure 1.1: Schematic illustrating physical domain (left) and the numerical interpretation (right). A well bore is drilled horizontally through the bitumen pay zone that supplies thermal energy (electro magnetic) and a solvent (propane) to mobilize and displace bitumen deposits.

For all of near wellbore flow cases, the 2D assumption is utilized as L is sufficiently large to neglect end effects. As a result, the depth taken in the z direction is simply one unit depth, $1m$. Though pressure drop along the injector well bore as well as pressure drop throughout the domain would likely impact on the saturation temperature, it is assumed to be constant. The pressure drop throughout the domain for most cases has been observed to result in a maximum change in saturation temperature on the order of a few degrees Kelvin.

1.1 Literature Review

This section will include an overview of relevant topics and studies in the field of modelling two-phase flow in porous media and phase change. A description of conventional techniques used to model diffusive interface transport in porous media using saturation functions, irreducible saturations of each respective phase etc. will be followed by a description of this study and how assumptions made allow for a deviation from such standard methodologies. Finally, a brief overview of numerical phase change methodologies will follow in order to establish an understanding of the tools available to model such a process.

1.1.1 Multiphase Flow in Porous Media

The study of multicomponent mass transfer is of increasing interest as this topic is the basis of a wide variety of industrial applications. These applications include drying in porous media [8], oil recovery and geothermal applications [9, 10], heat pipes [11], groundwater contamination [12, 13] etc. [14, 15]. Great efforts have been devoted over the years to develop Multiphase Flow Models where each phase is represented by its own momentum and mass conservation equation where inferfacial boundary conditions are imposed at each phase boundary [16, 17]. More recently Multiphase Mixture Models have been developed where mass and momentum conservation is imposed by solving a single equation for each phase respectively since all of the fluids are governed by the same equations [15] where the mixture properties are calculated based on a volume averaging of the phase composition in each cell. The flow of each phase respective to one another is determined in part by knowledge of relative permeabilities to account for the presence of other phases and the inherent decrease in effective flow area. Experimental studies must be conducted to quantify the relative permeabilities of each phase and can be dependent on many parameters including the specific fluid pairing, porosity, base permeability of the porous media, flowrate, etc.

[18]. An irreducible saturation of a given phase, or the amount of phase "a" that remains when when it is displace by phase "b", obstructs the flow of the other phase and must also be determined experimentally.

This study Considers the phases to be fully immiscible and a completely reversibly saturatable in the porous matrix such that the use of relative permeabilities and irreducible saturations need not be considered such that the use of the VOF method can be implemented with some modifications to the governing equations. Karim *et al.* [19] studied wave interaction with a porous zone and demonstrated agreement between numerical and experimental results without the use of such flow functions. The imbibition, or displacement of a phase boundary, of a liquid phase in a porous structure using the VOF method was demonstrated by Carciofi *et al.* [20] where in initial gaseous pocket was displaced by the progression of a sharp interface driven by an imposed pressure gradient. Numerical findings compared well with the Lucas-Washburn and Darcy's law equations in radial coordinates. Other work in this area demonstrate the applicability of sharp, immiscible interfaces in porous media [21, 22].

1.1.2 Phase Change

Many great efforts have resulted in a wide variety of methodologies used to handle the interfacial boundary constraints defining a multiphase flow undergoing phase change. In most cases, the algorithms used to advect the interface are largely interchangeable where the determination of how the coupling boundary conditions at the interface define the uniqueness and novelty of the solver. Most interfacial advection algorithms calling for the use of geometric interface reconstruction and coupling between interface tracking methodologies (Coupled Level-Set Volume of Fluid [23]) typically result in a more robust solver through the reduction of flotsam/jetsam, parasitic currents, and finally reduction in demand for an excessive grid resolution [24, 25, 26]. The use of the Level-Set method is used widely as the smoothed interface transition allows for the accurate calculation of the interface normal and consequently, the curvature of the interface for the surface tension force [27] [28] [29]. Many authors have utilized the VOF method to track the moving the interface [30] and some who utilize some special treatment of calculations involving the interface normal/curvature [31, 32, 33, 7]. Other authors intimately link the advection of both a LS field and a VOF field in a method known as the Coupled Level-Set Volume of Fluid (CLSVOF) method along with interface reconstruction to benefit from a smooth interface transition, improving the interface curvature calculations and from mass conservation respectively [34, 35]. A less rigorous and less accurate methodology known as the Simple-CLSVOF (SCLSVOF) method has been studied [36] that eliminates the need for interface reconstruction.

Independent of the advection algorithm used for the interface transport is the quantification of the mass flux due to phase change. Two interfacial boundary conditions (described in the next chapter) for heat transfer must be satisfied at the interface in order to maintain the physical nature of the phase change process. Imposing these boundary conditions s not done explicitly as a `slip` or `noSlip` condition would be for wall boundary; instead, the conditions are imposed implicitly by either 1) measuring heat fluxes into and out of the interface [27, 28, 30, 34, 35, 29] or by 2) *marking* cells in the liquid phase that are not satisfying the interfacial boundary condition, i.e. when $T_{interface} \neq T_{sat}$, and *penalizing* them through heat of vaporization, thereby correcting the interface temperature [37, 38, 31, 32, 33, 7, 36, 39].

This study exploits the use of penalizing the interface cells that deviate from the saturation temperature as this ensures the interface satisfies the boundary constraint. Quantifying the rate of phase based on an excess temperature, or deviation from the saturation temperature, may seem somewhat arbitrary, however, if implemented with the proper temporal resolution and correct scaling factors (described in the next chapter), satisfying the saturation temperature boundary constraint results in a satisfying the other Neumann interfacial boundary constraint as the remainder of the physics behave in a manner consistent with the physics of phase change. It has been observed in this study, though it has not been presented in this thesis, that measuring the heat fluxes across the interface to quantify the mass flux does not guarantee the interfacial temperature remains at the saturation temperature. This method, without the use of any of the interface reconstruction techniques described above, is also plagued by the same difficulties related to the quantification of the interface curvature for determining the surface tension forces in the momentum equation, i.e. since the normal component of the heat flux into the interface must be determined, the measurement of the interface normal must be accurate, requiring the use of interface reconstruction or coupling between advection algorithms. It is this very reason that traditional VOF methodologies are limited by the presence of parasitic currents and flotsam/jetsam when using density ratios common to two phase configurations commonly seen when considering immiscible, vaporizing two-phase flows. A review of phase change methodologies is presented by Lee *et al.*.

1.1.3 Phase Change in Porous Media

Various authors have combined the methodologies of modelling multiphase flow in porous media with the effects of phase change and heat transfer. With the current availability of open source software capable of modelling complex multiphase flows out of the box, advances in developing multi-physics solvers have been rapid. Beckermann *et al.* [40] considered the progression of a melting/freezing in the presence of natural convection and porous media. Though the explicit tracking of the interface did not require the solution of an advection equation since the location of the interface was dependent on the temperature relative to the saturation temperature. Tomar [41] considered the effect of saturation diffusion and relative permeabilities in a simulation considering the imbibition of a liquid phase into a constantly heated porous channel. His study considered, for a variety of heat fluxes and wall super-heat temperatures, the flow characteristics of the liquid through the porous matrix. A review of some established methodologies and work in the area of phase change in porous media can be found by Yortsos *et al.* [42].

This study incorporates the effects of phase change utilizing volume averaging and the penalization method in porous media including the transition from the free-flow portion of the domain to the porous zone. In the sections to follow, the governing equations and methodologies will be presented.

CHAPTER 2: PHASE CHANGE SOURCE TERMS: THE METHOD OF HARDT AND WONDRA

This section describes the method of Hardt and Wondra [6] for the application of modeling two-phase flow in the presence of phase change resulting from concentration gradients, excess temperature, etc. It should be noted that this study considers only the effects of excess temperatures, *i.e.* $T - T_{sat}$, where T_{sat} is assumed to be constant. For a vaporizing flow resulting from temperatures nearing the saturation temperature, two boundary conditions describe the frame work around which the phase change solver here is built. Equation 2.1 and 2.2 respectively, describe the Dirichlet and Neumann conditions that a macro-scale two phase system must abide.

$$T_{int} = T_{sat} \tag{2.1}$$

$$-k_v \frac{\partial T_{v,int}}{\partial n} = -k_l \frac{\partial T_{l,int}}{\partial n} + \dot{m} h_{fg} \tag{2.2}$$

Here, $n = \nabla\alpha/(\sqrt{\nabla\alpha})^2$, is the interface normal, where α is the VOF field indicating the fractional volume of fluid in any given cell. Since the interface is not constrained to be fixed in space at any point in time, prescribing either of these conditions cannot be done explicitly. For this study, the Dirichlet condition is imposed *implicitly* by marking cells in the interface region that deviate from the saturation temperature, providing a basis for quantifying rate of phase change. The indicated interface cells are *penalized* through latent heating where the Neumann condition is inherently satisfied as a result of solving the energy equation enforcing the conservation of energy. Before describing the source terms, their quantification and how they are distributed, some fundamental fields will be described in greater detail.

To track a moving interface, a VOF/indicator field is advected throughout the domain, providing a means for tracking the interface, determining material properties, etc. Since the source terms must be determined by fundamental algebraic operations on the available fields and should be distributed around the moving interface, the VOF field becomes a primary candidate for marking the interface region. Fig.2.1 depicts the VOF field, α, and some derived fields based on α that are described below.

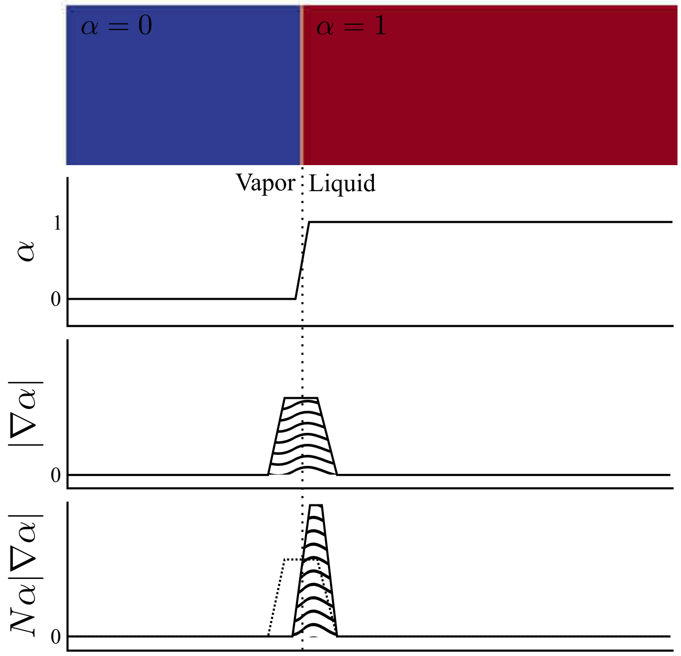

Figure 2.1: Schematic illustrating the VOF field, α, and derived fields. The line plots depict the manner in which the phase change source terns are shifted into the liquid phase by α and are scaled by N such that the areas under the last two curves are equal.

One key feature of using α is its physical significance.

$$\iiint_V |\nabla\alpha| dV = \int_S dS \tag{2.3}$$

The above equation states that the integral on the LHS is equal to the arc length of an interface in 2D or the surface area of an interface in 3D. Since Eq.2.3 describes a physically meaningful quantity, shifting the field into the liquid phase with α (Fig.2.1) calls for the calculation of a correction factor, N, such that Eq.2.3 holds true for the shifted field. Though some simulations are presented in 2D, they are treated numerically as a 3D problem with an arbitrary depth in the infinite direction. This being the case, $|\nabla\alpha|$ can be interpreted as the interfacial area per unit volume, supporting Eq.2.3. Since it is evident that α bares significance beyond simply marking the volume of fluid in a given cell, it will be used to develop the phase change source terms.

2.1 Quantifying the Rate of Phase Change

As described above, an excess temperature will be the driving potential in this phase change model. Suppose that the solver sees an excess temperature in a region containing the interface, a location where $T - T_{sat} > 0$ Eq.2.4.

$$C(T - T_{sat})|\nabla\alpha| \tag{2.4}$$

Upon inspection, and assuming for now that C is some constant with units of $kg/(sm^2K)$, it is clear that Eq.2.4 identifies regions where the Dirichlet condition in Eq.2.1 is un-satisfied. It is also important to note that the interfacial region contains both liquid and vapor. This can be seen in the second line plot in Fig.2.1. In a vaporizing flow, the vapor must to be superheated (or subcooled) where the liquid phase should remain near the saturation temperature. It should be important to note that small scale deviations in the interface temperature are important to model, for example, in contact line vaporization studies where length scales are small. For this study, most length scales considered are on the order of tens of millimeters up to meters. So in order to be more consistent with this fact, we mark the regions where Eq.2.1 is un-satisfied by shifting $|\nabla\alpha|$ into the liquid phase where the super-heating of the liquid phase is of interest. This shifting process is demonstrated in the last line plot in Fig.2.1 where α is used to shift the source term to the liquid phase and N is used to ensure the area under the curves in Fig.2.1 are equal. Based on this principle, Eq.2.5 is the driving potential for this phase change solver as it identifies regions of the interface that are deviating from the saturation temperature, and therefore, must be corrected by the liberation liquid and cooling the interface through the latent cooling.

$$\dot{m}_o = N\alpha C(T - T_{sat})|\nabla\alpha| \tag{2.5}$$

While α in Eq.2.5 is utilized to shift the source term into the liquid phase, $\iiint_V |\nabla\alpha| dV$ becomes attenuated as we have truncated the majority of the vapor side of the interface. In order to preserve the physical meaning of $|\nabla\alpha|$, a correction factor, N, is calculated to compensate for the shift.

$$\iiint_V |\nabla\alpha| dV = N \iiint_V \alpha|\nabla\alpha| dV \tag{2.6}$$

N ensures the integrands in Eq.2.6 on either side are equal and is calculated at each time step. The source term distribution is present only in regions containing the interface, *i.e.* when $0 \leq \alpha \leq 1$; theoretically, confining the source terms in the interface region is physical but becomes impractical to model numerically since the interface may only transition over one cell, resulting in a narrow band of source terms distributed at the interface which can lead to instability, especially on finer grids. In order to mitigate this issue, the sharp source term distribution if diffused, or smeared, over a few computational cells on either side of the interface by solving an in-homogeneous Helmholtz equation for a smeared source term distribution, $\dot{m}_{o,diffuse}$.

$$\nabla^2 \dot{m}_{o,diffuse} = \frac{1}{D\Delta t}(\dot{m}_{o,diffuse} - \dot{m}_o) \tag{2.7}$$

Equation 2.7 will diffuse the source term field in a conservative way since the boundary conditions prescribed for this operation are `zeroGradient`. Some aspects regarding the diffusion length/time scale ($\frac{1}{D\Delta t}$) are very important to consider as enough diffusion should be allowed such that these instabilities can be overcome but no so much that the source terms are distributed too far from the interface, resulting in a less physical model.

Finally we have arrived at the final forms of the source term describing this vaporizing flow. $\dot{m}_{o,diffuse}$ describes only the local rate of mass to change phase per unit volume, it does not determine the mass source and mass sink distribution necessary to model the vaporizing flow. Another source term, $\dot{m}$, is introduced which distributes the magnitude of $\dot{m}_{o,diffuse}$ to either side of the interface to account for mass appearing in the vapor phase and mass disappearing from the liquid phase.

$$\dot{m} = \dot{m}_{o,diffuse}(N_v(1-\alpha) - N_l\alpha) \tag{2.8}$$

N_v and N_l are constants and are determined in a manner similar to N such that the net rate of mass appearing is equal to the net rate of mass disappearing and both are equal to the total quantity of mass to change phase determined by $\dot{m}_o$.

$$\iiint_V \dot{m}_o dV = N_v \iiint_V (1-\alpha)\dot{m}_{o,diffuse} dV \tag{2.9}$$

$$\iiint_V \dot{m}_o dV = N_l \iiint_V \alpha\dot{m}_{o,diffuse} dV \tag{2.10}$$

Kunkelmann [7] reported an alternative to distributing the source terms in Eq.2.8 that follows the same procedure described above. The use of a Heaviside function and a cut-off threshold, $F_{cut} = 1e{-}3$, is used to eliminate source terms in the transition region of the interface, $(0+F_{cut}) \leq \alpha \leq (1-F_{cut})$.

$$\dot{m}_{HS} = \dot{m}_{o,diffuse}(N_{v,HS}H(F_{cut}-\alpha) - N_{l,HS}(\alpha - 1 + F_{cut})) \tag{2.11}$$

The updated values of correction factors, $N_{v,HS}$ and $N_{l,HS}$, are modified using a Heaviside function centred about 0.

$$\iiint_V \dot{m}_o dV = N_{v,HS} \iiint_V H(F_{cut}-\alpha)\dot{m}_{o,diffuse} dV \tag{2.12}$$

$$\iiint_V \dot{m}_o dV = N_{l,HS} \iiint_V H(\alpha - 1 + F_{cut})\dot{m}_{o,diffuse} dV \tag{2.13}$$

The fields discussed in this section are illustrated in Fig.2.2. It is important to note the shift in $\dot{m}_o$ between panels b) and c). If the initial source term weren't shifted into the liquid phase, the behavior of the vaporizing flow would be much different.

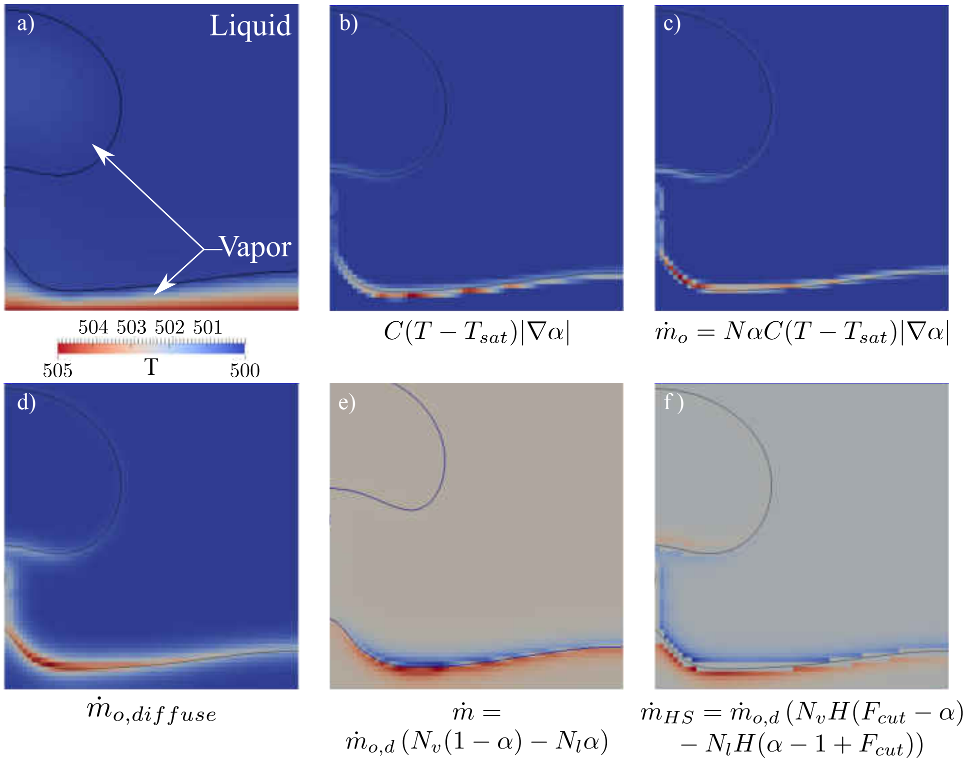

$C(T - T_{sat})|\nabla\alpha|$

$\dot{m}_o = N\alpha C(T - T_{sat})|\nabla\alpha|$

$\dot{m}_{o,diffuse}$

$\dot{m} = \dot{m}_{o,d}\,(N_v(1-\alpha) - N_l\alpha)$

$\dot{m}_{HS} = \dot{m}_{o,d}\,(N_v H(F_{cut} - \alpha) - N_l H(\alpha - 1 + F_{cut}))$

Figure 2.2: **a)** Superheated vapor film supplying thermal energy to a saturated interface from a boundary at a constant excess temperature. **b)** Initial quantification of the rate of phase change based on temperature superheat. **c)** Shifting the field found in b) to the liquid side of the interface to recover a more meaningful quantity, Eq.2.5. **d)** Diffusion of the field found in c) for the distribution of the source terms on either side of the interface while decreasing the peak magnitude of the source term, aiding in numerical stability (Eq.2.7). **e)** Distributing the source terms on either side of the interface to construct the source term (Eq.2.8) present in the pressure equation (Eq.3.3). **f)** Same as e) but incorporating the changes proposed by Kunkelmann [7] (Eq.2.11).

The interpretation of C, with units of $kg/(m^2 sK)$ takes the form of a resistance to mass transfer ($C = 1/R$) where the excess temperature is the driving potential. Tanasawa [38] reported a method of determining the magnitude of this value as well as a table containing experimentally determined values of an essential empirical constant for various fluids. In the current study, it has been shown that accuracy can be ensured by sufficiently increasing this value until convergence is met. One can also think of decreasing the resistance to mass transfer, i.e. by increasing C. Theoretically, maintaining the interface at the saturation temperature is a necessary condition to maintain a boiling flow. Increasing the value of C will result in a rapid system response to any deviation of the interface temperature from T_{sat}. This mechanism ensures the interfacial boundary constraint remains imposed my minimizing the magnitude of $T - T_{sat}$ through the liberation of liquid and consumption of latent heat, thereby cooling the interface to the imposed saturation temperature. The opposite holds true for condensation as well.

The section to follow describes the governing conservation equations of momentum, mass and energy along with the VOF equation.

CHAPTER 3: GOVERNING EQUATIONS

This section provides the governing equations for a vaporizing, immiscible two-phase system in a heated domain comprised of free and porous media. Since this model assumes incompressibility, the mixture properties are simply a mixture average based on the VOF field, *i.e.* $()_f = \alpha()_l + (1-\alpha)()_v$ where the subscripts f, l and v denote the property associated with the fluid mixture, liquid and vapor respectively and the parenthesis represent some material property such as density, viscosity, etc.

3.1 Momentum Equation in Porous Media

Flow in porous media requires special treatment due to the presence of the rigid porous matrix through modification of the typical terms and the inclusion of an additional flow resistance term proportional to the fluid velocity.

$$\begin{aligned}\frac{\rho}{\chi}\left(\frac{\partial \mathbf{u}}{\partial t} + (\mathbf{u}\cdot\nabla)\frac{\mathbf{u}}{\chi}\right) = \nabla\cdot\left[-p\mathbf{I} + \frac{\mu}{\chi}\left(\nabla\mathbf{u} + (\nabla\mathbf{u})^T\right)\right] + \\ \rho\mathbf{g} + \mathbf{F_{st}} - \frac{\mu}{\Pi(\chi)}\mathbf{u}\end{aligned} \tag{3.1}$$

Eq.3.1, the momentum equation, utilizes the Darcian velocity which is volume averaged and incorporates the zero velocity of the fixed solid [43]. This form of Eq.3.1 is an extension of Darcy's law incorporating local fluid acceleration through the porous media [3] and also a diffusion term required for the modelling of forces resulting from shear stresses [4]. The interstitial pore velocity, $\mathbf{U}$, in the transient and convective terms can be recast from the Dupuit-Forcheimer relation:

$\mathbf{U} = \mathbf{u}/\chi$ where χ is the porosity. The convective term is typically neglected due to its low magnitude relative to the drag term arising from Darcy's law (last term on the RHS), however it is necessary to retain this term to handle transitions to higher porosity structures, or in the limiting case, when $\chi \rightarrow 1$ for free flow. A similar argument can be made for the viscous diffusion term since its presence is commonly considered to be inappropriate in most low porosity media since the mechanisms of the evolution of shear stresses in a fluid element do not apply exactly when volume averaging is utilized. This form of the momentum equation, applicable for multiphase flow with mixture properties, is presented by Hsu and Cheng [5] and Le Bars and Worster [43] where the Forcheimer term, $c_F K^{-1/2} \rho_f |\mathbf{u}|\mathbf{u}$, is dropped assuming low Re flow.

3.2 Interface Capturing and Continuity

The advection of the liquid/vapor interface is captured by a simple scalar conservation equation known as the Volume of Fluid (VOF) equation.

$$\frac{\partial \alpha}{\partial t} + \nabla \cdot (\boldsymbol{u}\alpha) - \alpha \nabla \cdot \boldsymbol{u} = 0 \tag{3.2}$$

The form of the continuity equation remains largely unaffected where the Darcian velocity is utilized in ensuring mass conservation. The divergence in the velocity field resulting from phase change is introduced in the RHS of Eq.3.3 where $\dot{m}$ is the mass source term arising from the vaporization/condensation of the liquid/vapor phases at the interface.

$$\nabla \cdot \mathbf{u} = \frac{\dot{m}}{\rho_f} \tag{3.3}$$

Using Eq.3.3 to substitute into the last term of Eq.3.2 while accounting for the presence of the porous matrix by modifying the transient term with χ, the VOF equation can be written as follows:

$$\frac{\partial \chi \alpha}{\partial t} + \nabla \cdot (\boldsymbol{u}\alpha) = \alpha \nabla \cdot \boldsymbol{u} = \alpha \frac{\dot{m}}{\rho_f} \tag{3.4}$$

The manner in which porosity is added accounts for the fact that the Darcian/volume averaged velocity field is utilized to move the interface instead of the *actual*, intrinsic pore velocity per the Dupuit-Forcheimer relation. Weller [44] introduced an artificial compression term that remains active only at the interface to offset the effects of numerical diffusion arising from the advection of a sharp scalar field. It is important to note the last two terms in Eq.3.4 are theoretically identical, however, their numerical implementation results in subtle differences resulting from the breakdown of the numerical solution procedure and therefore, the use of $\nabla \cdot \boldsymbol{u}$ is preferred as it is more consistent with the numerics of the problem. Treating the porosity as a constant, we have:

$$\frac{\partial \alpha}{\partial t} + \frac{\nabla \cdot (\boldsymbol{u}\alpha)}{\chi} + \frac{\nabla \cdot (\alpha(1-\alpha)\boldsymbol{u}_c)}{\chi} = \frac{\alpha \nabla \cdot \boldsymbol{u}}{\chi} \tag{3.5}$$

α is a scalar field used to indicate liquid ($\alpha = 1$) and vapor ($\alpha = 0$). The RHS of Eq.3.5, typically zero in the absence of phase change, is retained and allows for the removal of liquid/vapor due to the divergence in the flow field added by the mass source term in Eq.3.3. The material property fields are determined using the rule of mixtures where the subscripts l and v refer to liquid and vapor phases respectively, e.g. $\rho_f = \alpha\rho_l + (1-\alpha)\rho_v$. α must remain bounded ($0 \leq \alpha \leq 1$) in order to accurately track a moving interface due to the manner in which the material properties are distributed across the interface. This is accomplished in part by using a Flux Corrected Transport algorithm based on Zalasek's method [45] known as MULES, a standard feature developed by OpenFOAM.

3.3 Energy Equation

The conservation of energy is applied to both the solid and fluid phases. The energy equation is presented for solid matrix

$$(1-\chi)\frac{\partial(\rho C_P T)_s}{\partial t} = (1-\chi)\nabla\cdot(k_s \nabla T_s) + (1-\chi)q_s''' \tag{3.6}$$

and for the fluid

$$\begin{aligned}\chi\frac{\partial(\rho C_P T)_f}{\partial t} + \chi\nabla\cdot(\rho C_P \boldsymbol{U} T)_f &= \\ \chi\nabla\cdot(k_f \nabla T_f) + \chi q_s''' + \chi(C_P T)_f &\left[\frac{\partial \rho_f}{\partial t} + \nabla\cdot(\rho \boldsymbol{U})_f\right]\end{aligned} \tag{3.7}$$

Since a large quantity of particles are contained within a given computational cell, and the particle surface area to volume ratio is large, i.e. small solid particles, it can be assumed that the liquid phase and solid phase exist in thermal equilibrium. Along with the assumption of thermal equilibrium, heat conduction is assumed to occur in parallel through both phases and transitions from free flow to porous media are neglected. Substituting the Dupuit-Forcheimer relation, the energy equation becomes the volume average of Eqs.3.6 and 3.7.

$$\begin{aligned}\frac{\partial(\rho C_P T)_{eff}}{\partial t} + \nabla\cdot(\chi\rho C_P \frac{\boldsymbol{u}}{\chi} T)_f &= \\ \nabla\cdot(k_{eff}\nabla T) + q_{eff}''' + (C_P T)_f &\left[\frac{\partial \chi\rho_f}{\partial t} + \nabla\cdot(\chi\rho\frac{\boldsymbol{u}}{\chi})_f\right]\end{aligned} \tag{3.8}$$

Here, q'''_{eff} represents sources due to phase change, volumetric heat generation, etc. and since the assumption of thermal equilibrium is applied, the subscript will be dropped. The source term on the RHS of Eq.3.8 would vanish in the case of no phase change since it is equivalent to the continuity equation for a compressible flow. Instead of substituting $\dot{m}/\rho_f$ (RHS of Eq.3.3) in place of this term, which would be a valid substitution, the terms are calculated explicitly and are treated as *known* source terms. This is a direct consequence of the numerical solution procedure and the decomposition of the algorithm into steps (see next chapter). In the case where phase change is present, the continuity equation takes care of the flow field pressure and velocity and the VOF equation takes care of the artificial removal of α to account for the disappearance of liquid during vaporization. Since the solution of the energy equation follows the advection of the interface, the source term explicitly calculated and added in the energy equation. This source term must be accounted for in the energy equation or else this change in internal energy between phases ($\rho C_{P,liquid} \neq \rho C_{P,vapor}$) by the removal of liquid at the interface results in a divergence in the temperature field. Assuming constant material properties, the energy equation becomes

$$\begin{gathered}\frac{\partial(\rho C_P T)_{eff}}{\partial t} + \nabla\cdot(\rho C_P \boldsymbol{u} T)_f = \\ \nabla\cdot(k_{eff}\nabla T) + q''' + T\left[\frac{\partial(\rho C_P)_{eff}}{\partial t} + \nabla\cdot(\rho C_P \boldsymbol{u})_f\right]\end{gathered} \tag{3.9}$$

Note that $\partial(\chi\rho C_p)_f/\partial t = \partial(\rho C_p)_{eff}/\partial t$ since the porous matrix is rigid with constant properties and the only changes in ρC_P result from the movement of the interface in this Eulerian formulation. $\partial(\chi\rho C_p)_f/\partial t$ is then replaced by $\partial(\rho C_p)_{eff}/\partial t$ to eliminate additional redundant definitions.

CHAPTER 4: SOLUTION PROCEDURE

The development of the phase change solver presented here is built on the framework of an incompressible, two-phase flow solver for immiscible fluids in OpenFOAM. The solution procedure begins with the advection of the interface (Eq.3.5), followed by the calculation of source terms for phase change (Eqs.2.5-2.13 and procedure described by [6]), solution of the energy equation (Eq.3.9), updating the source terms again and finally updating the flow field while incorporating the source terms for phase change in Eq.3.3. The PIMPLE method is implemented here to solve for the unsteady velocity and pressure fields. The PIMPLE method consists of iteratively repeating the PISO/SIMPLE algorithm a prescribed number of times while relaxing the result between each PIMPLE iteration for a given time step. In other words, depending on the number of outer correctors specified (PIMPLE iterations), each time step is solved repeatedly while using the previous solution as an initial guess for the next outer loop cycle. Within the each step in the PIMPLE loop, the PISO/SIMPLE method calls for the solution of the momentum equation (Eq.3.1) using the pressure field from the previous time step where the result acts as a *predictor* to be used in the continuity equation. This *predictor* is then recast into a formulation in pressure and substituted into the continuity equation (Eq.3.3), referred to as the pressure equation, where an updated pressure field is determined. This pressure corrector process (PISO/SIMPLE) is repeated a specified number of times or until convergence with each pass of the outer corrector loop (PIMPLE). If the number of outer correctors used by the PIMPLE loop is reduced to `1`, the algorithm is reduced to the PISO/SIMPLE algorithm. Though this process dramatically increases the solve time in many cases, it has been observed to eliminate checker-boarding problems resulting from the use of collocated grids and `slip` conditions by simply increasing the number of outer loops from 1 (PISO/SIMPLE) to 2 (PIMPLE). A detailed explanation of the discretization procedure and solution of the momentum and pressure equations can be found in [46].

Validation cases in the sections to follow will demonstrate the robust nature of the implementation of the source terms developed by Hardt and Wondra [6] and the modification to $\dot{m}_{HS}$ using a Heaviside function and a cut-off threshold F_{cut} [7].

CHAPTER 5: VALIDATIONS

5.1 2D Channel Flow in Free and Porous Media

This section describes a Couette type flow where an imposed pressure gradient drives a single phase fluid through a domain comprised of a free flowing section and a porous media section divided symmetrically along the center of the domain, tangential to the flow direction, Fig5.1.

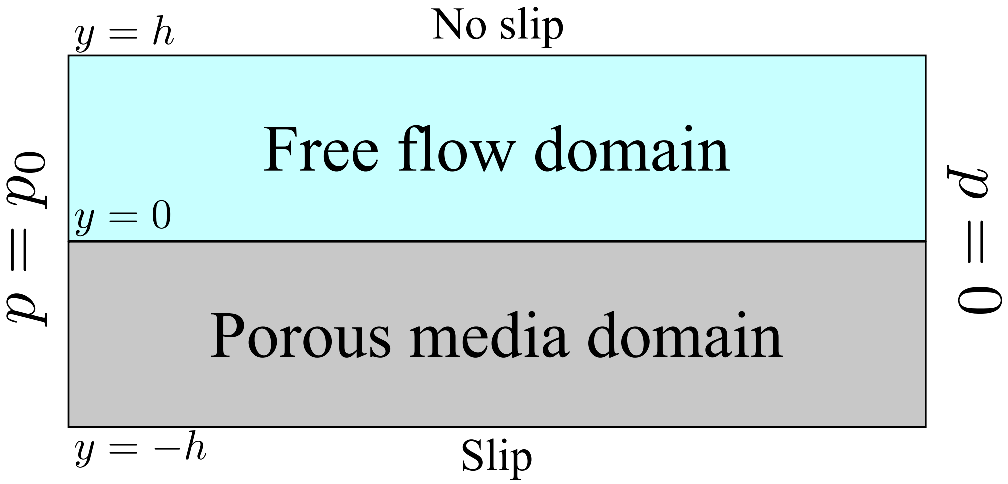

Figure 5.1: Computational domain schematic for the validation of the flow resistance term in the fluid momentum equation, Eq.3.1.

Eliminating the transient and convective acceleration term from Eq.3.1 for the single phase configuration results in a simplified momentum equation.

$$0 = -\frac{dP}{dx} + \frac{\mu}{\chi}\frac{d^2\boldsymbol{u}}{dy^2} - \frac{\mu}{\chi\Pi}\boldsymbol{u} \tag{5.1}$$

Eq.5.1 is solved subject to a `noSlip` and `slip` condition on the upper fixed wall and lower boundary respectively, Eq.5.2. It is also important to note that the permeability is a function of space such that Eq.5.1 reduces to the appropriate form when transitioning from free-flow to porous media.

$$\boldsymbol{u}(h) = 0\ ;\ \frac{d\boldsymbol{u}}{dy}(-\infty) = 0 \tag{5.2}$$

For the free flow portion of the domain, we determine the velocity profile:

$$u(y) = \frac{1}{2\mu}\frac{dP}{dx}(y-h)(y-A);\quad y > 0 \tag{5.3}$$

For the porous media section in the bottom half of the domain:

$$u(y) = Be^{y/\delta} - \frac{\chi\delta^2}{\mu}\frac{dP}{dx};\quad y < 0 \tag{5.4}$$

δ is defined as $\sqrt{\Pi/\chi}$ and the constants A and B are defined as:

$$A = -\frac{h\delta + 2\chi\delta^2}{h+\delta};\ B = -\frac{\delta}{2\mu}\frac{dP}{dx}\frac{h^2 - 2\chi\delta^2}{h+\delta} \tag{5.5}$$

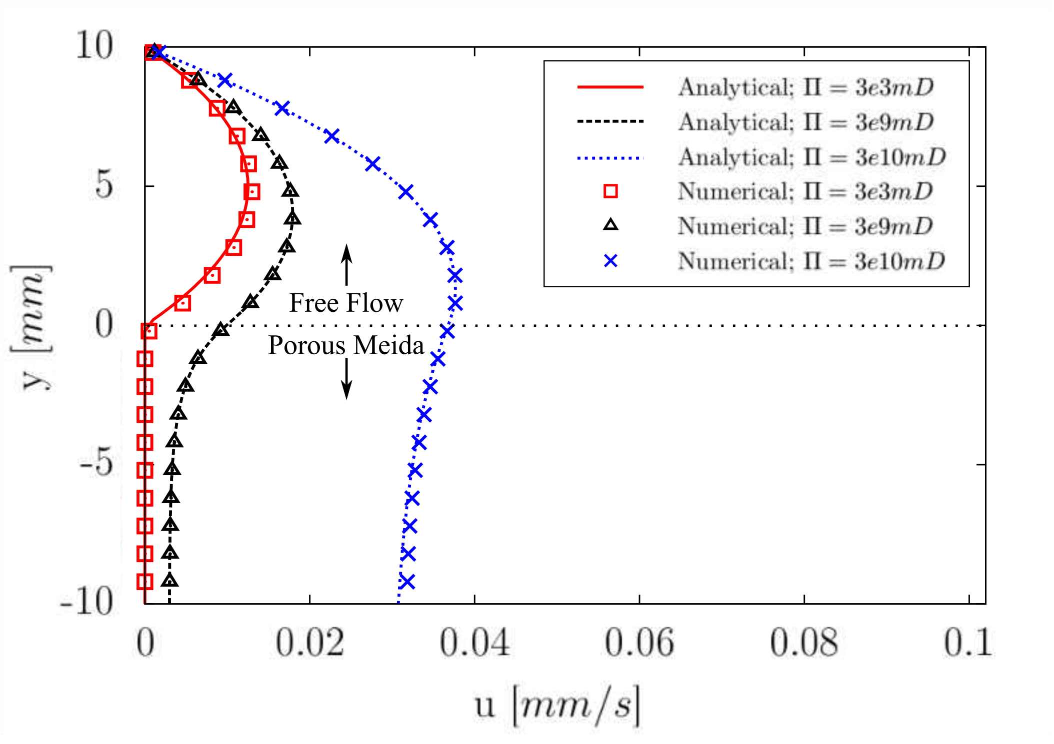

Figure 5.2: Velocity profiles along outlet of simulation domain for three values of Π and $\chi = 1$ over the entire domain.

For an imposed pressure gradient of $dP/dx = 0.001 Pa/m$, a porosity of $\chi = 1$ over the entire domain and a range of permeabilities in the porous zone, the outlet velocity profiles for water ($\rho = 1000$ and $\nu = 1 \times 10^{-6}$) are presented in Fig.5.2. It is clear that the results compare well with the theory for a range of permeabilities. The results presented here demonstrate the ability of the solver to not only model the presence of the porous media and the viscous flow resistance added by the porous media, but also the ability to handle transitions from porous to free flowing portions of the domain.

5.2 Stefan Problem

The phase change solver was benchmarked by comparison with solutions of analytical Stefan problems similar to those found in the literature [32, 47]. This study, however, considers sub-cooling of the liquid phase as well as the inclusion of porous media to illustrate the robust nature of the solvers performance. We first present the equations defining the Stefan problem with porous media and with arbitrary material properties. The governing equations here have been developed in a manner consistent with the volume averaging approach used to develop Eq.3.9.

$$\frac{\partial T_v}{\partial t} = \alpha_{Eff,v} \frac{\partial^2 T_v}{\partial x^2}; \;\; 0 \leq x \leq \delta(t) \tag{5.6}$$

$$\frac{\partial T_l}{\partial t} + \chi U_l \frac{\partial T_l}{\partial x} = \alpha_{eff,l} \frac{\partial^2 T_l}{\partial x^2}; \;\; \delta(t) \leq x < \infty \tag{5.7}$$

Equations 5.6-5.7 are solved using the adequate boundary and initial conditions and are coupled through Eqs.5.8, the interfacial boundary constraints.

$$T_v(0,t) = T_w \tag{5.8a}$$

$$T_l(\infty,t) = T_o \tag{5.8b}$$

$$k_{eff,l} \tfrac{\partial T_l(\delta(t),t)}{\partial x} - k_{eff,v} \tfrac{\partial T_v(\delta(t),t)}{\partial x} = \chi h_{fg} \rho_v \tfrac{d\delta}{dt} \tag{5.8c}$$

$$T_v(\delta(t),t) = T_l(\delta(t),t) = T_{sat} \tag{5.8d}$$

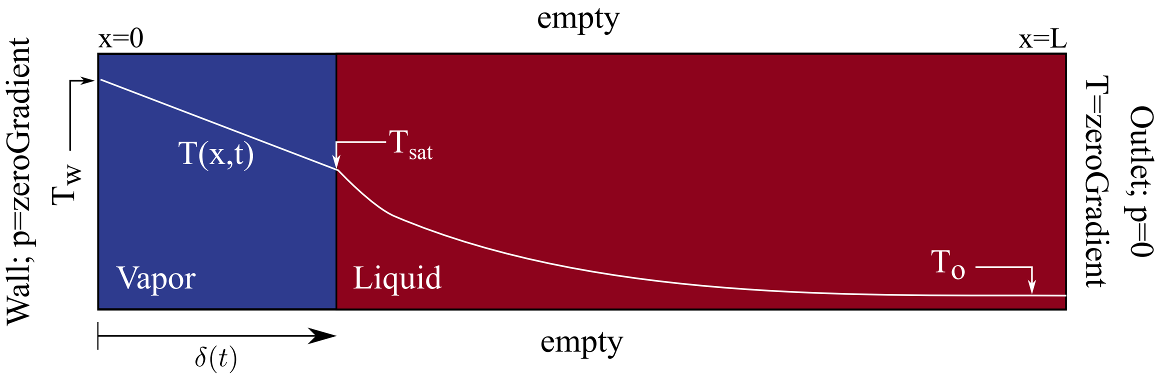

Figure 5.3: Schematic of Stefan problem identifying boundary conditions and configuration.

Note that Eq.5.8c is equivalent to Eq.2.2 where the product $\rho_v d\delta/dt \leftrightarrow \dot{m}$ are analogous, only with slightly different units resulting from dimensionality and the physical implementation of the source terms. Equations 5.6-5.8 describe the heat transfer in an initially infinitesimally small pocket of quiescent vapor separating a wall at $x = 0$ at a constant temperature, T_w, and an interface constrained to be at the saturation temperature, T_{sat}, Fig.5.3. As time progresses, heat conducts through the quiescent fluid and to the interface where the interfacial boundary constraint ensures that the discontinuity in the heat flux goes to cooling the interface through the latent cooling per Eq.5.8. If there is subcooling present, then the length of the simulation domain in the x direction must be large enough to behave in a semi-infinite manner to be consistent with the theoretical derivation and solution to this problem. Since the analysis is confined to the x direction only, mass conservation alone describes the flow and the manner in which U_x is defined. It is important to note that the velocities here are the interstitial pore velocities and therefore, Eq.5.8 must include χ to attenuate the rate of phase change since only a given void fraction of liquid exists in a cell containing both fluid and solid. Following Son [28], and with the addition of porosity for this study, the mass flux in the interface normal direction can be written in terms of the phase velocities and the interface velocity ($U_{int} = d\delta/dt$):

$$\dot{m} = \chi\rho_f(U_{int} - U_f) = \chi\rho_l(U_{int} - U_l) = \chi\rho_v(U_{int} - U_v) \tag{5.9}$$

After rearranging, we have:

$$U_l - U_v = \frac{\dot{m}}{\chi}\left(\frac{1}{\rho_v} - \frac{1}{\rho_l}\right) \tag{5.10}$$

For a quiescent vapor, $U_v = 0$. Substituting for $\dot{m}$ we have:

$$U_l = \rho_v U_{int}\left(\frac{1}{\rho_v} - \frac{1}{\rho_l}\right) \tag{5.11}$$

After simplifying, we have:

$$\rho_l U_l = U_{int}(\rho_l - \rho_v) = \frac{d\delta}{dt}(\rho_l - \rho_v) \tag{5.12}$$

where the interface velocity is simply $d\delta/dt = \lambda\sqrt{\alpha_{eff,v}/t}$ where the functional dependence of δ is assumed to be:

$$\delta(t) = 2\lambda\sqrt{\alpha_{eff,v}t} \tag{5.13}$$

Here, λ is an unknown constant to be determined. Now equipped with a set of equations coupled through the undetermined constant, λ, we can now solve Eqs.5.6 and 5.7 using the appropriate boundary conditions, initial conditions and expressions for $\delta(t)$ and U_l (Eqs.5.12 and 5.13).

$$T_v(x,t) = Aerf\left(\frac{x}{2\sqrt{\alpha_{eff,v}t}}\right) + T_w; \;\; 0 \leq x \leq \delta(t) \tag{5.14}$$

$$T_l(x,t) = T_o - Berfc\left(\frac{x}{2\sqrt{\alpha_{eff,l}t}} + \lambda\chi\frac{\rho_v - \rho_l}{\rho_l}\sqrt{\frac{\alpha_{eff,v}}{\alpha_{eff,l}}}\right); \;\; \delta(t) \leq x < \infty \tag{5.15}$$

$$A = \frac{T_{sat} - T_w}{erf(\lambda)} \tag{5.16}$$

$$B = (T_o - T_{sat})\Big/ erfc\left(\lambda\left[1 + \chi\left(\frac{\rho_v - \rho_l}{\rho_l}\right)\right]\frac{\sqrt{\alpha_{eff,v}}}{\sqrt{\alpha_{eff,l}}}\right) \tag{5.17}$$

Finally, applying the interfacial energy balance, Eq.5.8c, Eqs.5.14 and 5.15 are differentiated yielding the following transcendental equation in λ.

$$k_{eff,l}\frac{Be^{-\left(\lambda\sqrt{\frac{\alpha_{eff,v}}{\alpha_{eff,l}}}\left[1+\chi\left(\frac{\rho_v}{\rho_l}-1\right)\right]\right)^2}}{\sqrt{\pi\alpha_{eff,l}}} - k_{eff,v}\frac{Ae^{-\lambda^2}}{\sqrt{\pi\alpha_{eff,v}}} = \chi\rho_v h_{fg}\lambda\sqrt{\alpha_{eff,v}} \tag{5.18}$$

Given the material properties, Eq.5.18 can be solved numerically to determine the value of λ specific to the problem. Note that α in Eqs.5.6-5.18 is the thermal diffusivity. For cases where $\chi = 1$, i.e. when there is no porous media, these equations reduce to the appropriate form without and additional modifications.

5.2.1 Interfacial Mass Transfer Resistance: Choosing the Value of C

The first consideration made here is the mass transfer resistance term, $C = 1/R$. The value of C with units $kg/(sm^2K)$, determines how much mass of liquid will become vapor per every degree of superheat per second. Varying the value of C may seem to suggest that an infinite number of results can be determined for a given problem, yielding a somewhat arbitrary solution, however, this is not the case. Choosing a large value of C results in a stiff solver capable of resolving sudden transitions in interfacial temperature deviations. This requires greater temporal resolution to prevent excessive over and under-shooting the saturation temperature. For this section of the report, $\chi = 1$.

Table 5.1: Bulk phase material properties for Stefan validation problem.

	Property	Liquid	Vapor
ρ	Density ($\frac{kg}{m^3}$)	1	1
C_P	Specific Heat ($\frac{J}{kgK}$)	10	10
k	Thermal Conductivity ($\frac{W}{mK}$)	0.1	1
h_{fg}	Heat of Vaporization $= 1000\frac{J}{kg}$		
T_{sat}	Saturation Temperature $= 300K$		
T_w	Wall Temperature $= 305K$		
χ	Porosity (Free Flow) $= 1$		
λ	Stefan Constant $= 0.1568$ (Eq.5.18)		

For an arbitrary set of material properties (Tab.5.1), λ was determined from Eq.5.18 and the interfacial mass transfer resistance was varied similar to Kunkelmann [32] to determine the sensitivity

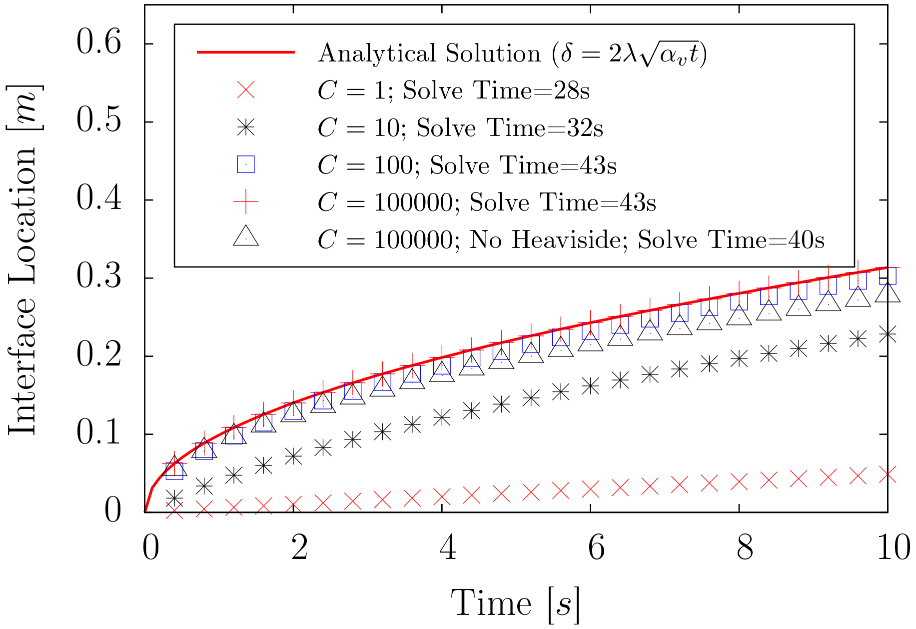

Figure 5.4: Interface location vs. time for various values of $C = 1/R$ compared to the exact solution without porous media.

of the solution to varying C. For a wall superheat of $5K$ and liquid initially at the saturation temperature, T_{sat}, the numerical results for the interface location with respect to time is compared with the Stefan solution in Fig.5.4.

The results demonstrate convergence on the analytical solution by decreasing the interfacial resistance to mass transfer (R), i.e. increasing the value of C. Also, the use of Eq.2.8 (triangles in Fig.5.4) results in a large error when compared to the method of Kunkelmann [7], Eq.2.11 (every other case in Fig.5.4). It should be noted that the solution run time increased as C increased; this is a result of a decrease in response time required to resolve deviations of the interface temperature from the saturation temperature. The use of excessively large values of C often result in oscillations in the temperature at the interface and can result in inconsistent results that require this type of increased temporal resolution to smooth out. This solver utilizes the fluid Courant number and the interface Courant number to establish criteria for determining the time step which include the effects of grid size distribution. Though these criteria tend to remove the user from tedious trouble shooting by setting these governors at a conservative value, it has been observed that a maximum allowable time step can be set to ensure the solver can properly resolve the physics of phase change during the solution process. The limit of this maximum allowable time step is dependent on the aforementioned physics as well as the temporal and spatial resolution. For the time being, qualitative inspection of the temperature at the interface and C independence (Fig.5.4) has been an adequate measure for ensuring a converged solution on a particular grid. The dependence of C on grid and temporal resolution will be a focus of future work.

5.2.2 Stefan Problem using Propane

For this portion of the study, results including saturated liquid/vapor propane at $1.75MPa$, Tab.5.2, will be considered where the properties are assumed to be constant in the bulk phases due to the relatively small temperature range. For this section of the report, $\chi = 1$.

Table 5.2: Bulk phase material properties of propane at the saturation pressure of $1.75MPa$ [48].

	Property (Propane at $1.75MPa$)	Liquid	Vapor
ρ	Density ($\frac{kg}{m^3}$)	446.55	39.77
C_P	Specific Heat ($\frac{J}{kgK}$)	3067.37	2431.02
k	Thermal Conductivity ($\frac{W}{mK}$)	0.081	0.024
h_{fg}	Heat of Vaporization $= 420 \times 10^3 \frac{J}{kg}$		
T_{sat}	Saturation Temperature $= 324.1K$		
T_w	Wall Temperature $= 305K$		
χ	Porosity (Free Flow) $= 1$		
λ	Stefan Constant $= 0.0991$ (Eq.5.18)		

It should be noted that the heat of vaporization in the case of propane is at least two orders of magnitude higher than the fictitious fluid used for the case of Fig.5.4. As a result, more energy is required to convert the same volume of fluid to vapor and consequently, the length scales in the simulation must be decreased in order to resolve the slowly vaporizing interface to obtain a result that is comparable with the analytical solution.

For this validation, a similar procedure is followed, however, the initial temperature of the liquid

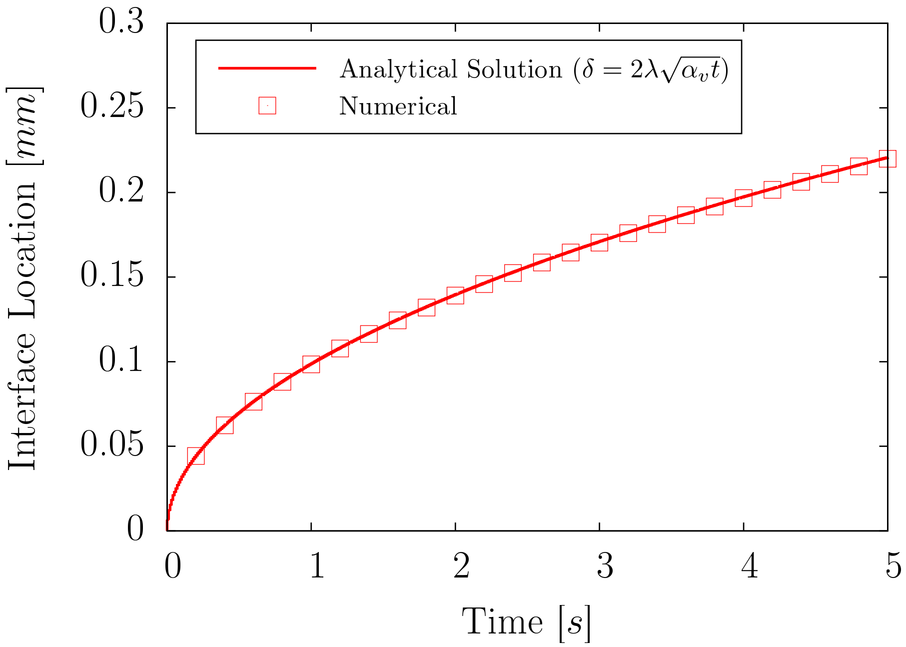

Figure 5.5: Interface location vs. time for liquid/vapor propane at $1.75MPA$ compared to the exact solution without porous media.

phase is subcooled by $2K$ to assess the abilities of the solver and the implementation of the phase change source term distribution developed by [6] to handle the sub-cooling of the liquid at the interface. 6000 cells uniformly distributed to ensure the most accurate solution possible were utilized to define the problem. For the scenario described in the previous validation but with propane as the material, the validation demonstrates excellent agreement with the theory, Fig.5.5.

Recalling the expression for the interface velocity, the liquid velocity is defined as $U_{int} = U_f + \dot{m}/\rho_f = \dot{m}/\rho_v \rightarrow U_l = U_{int} - \dot{m}/\rho_l = \dot{m}(1/\rho_v - 1/\rho_l)$. Noting that $\dot{m} = \rho_v U_{int} = \rho_v d\delta/dt = \lambda\rho_v\sqrt{\alpha_v/t}$, the liquid velocity can be expressed as $U_l = \lambda(1 - \rho_v/\rho_l)\sqrt{\alpha_{eff,v}/t}$. It is clear that in the case of equal densities ($\rho_v = \rho_l$), the liquid velocity would diminish and the problem would resemble that of a melting/freezing problem noting that for the latter, the sign of the RHS of Eqs.5.8 and 5.18 would change due to the sign associated with the latent heating. Table 5.3 compares the numerical results for the liquid velocity to the analytical expression described above.

Table 5.3: Bulk phase material properties of propane at the saturation pressure of $1.75MPa$ [48].

Time	Analytical Velocity ($\frac{mm}{s}$)	Numerical ($\frac{mm}{s}$)
$t = 0.1s$	0.143	0.142
$t = 1s$	0.045	0.045
$t = 5s$	0.020	0.020

Excellent agreement between the simulation and theory is evident by comparison. The numerical prediction of the velocity is slightly under predicted for the early times in the simulation as a result of the manner in which the problem is solved numerically. The theory requires the interface to be located at $x = 0$ at $t = 0$. The numerical problem must be formulated with a finite amount of vapor near the wall to set the solution marching forward. It is this vapor pocket, set to be the average between the wall and saturation temperature that results in a lagging of the progression of the interface and, consequently, a slight under prediction in interface position as well as the liquid velocity. The theoretical temperature distributions from Eqs.5.6 and 5.7 are also used to verify the solvers performance and are found in Fig.5.6.

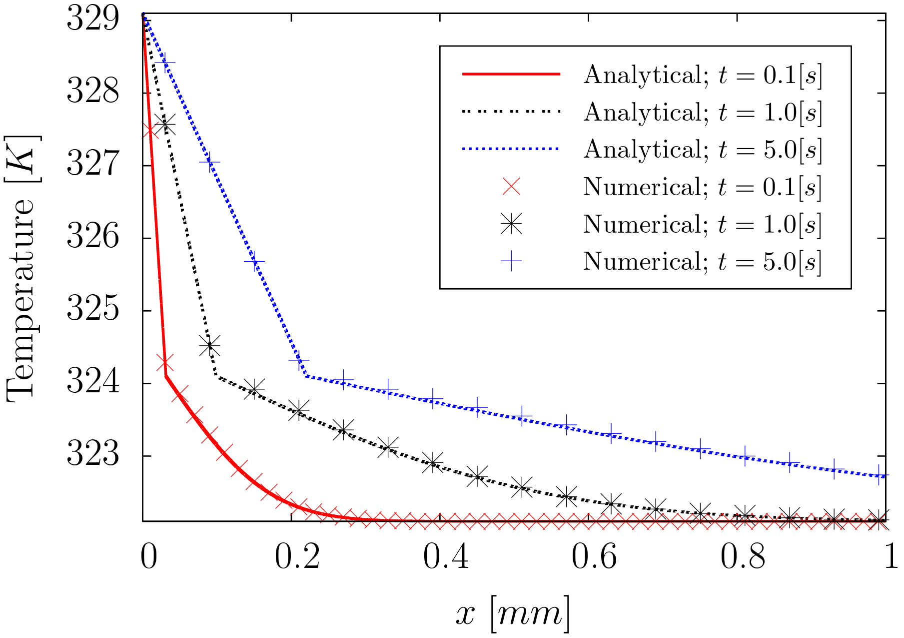

Figure 5.6: Temperature distributions for liquid/vapor propane at $1.75MPA$ in the vapor (left of discontinuity) and liquid phase (right of discontinuity) compared to the exact solution without porous media.

The temperature distribution clearly abides Eqs.5.6 and Eq.5.7 made subject to the interfacial boundary constraint (Eq.5.8) where the temperature remains saturated. It should also be noted that $1mm$ of domain is presented here for visualization; however, $3mm$ of domain was required to model the semi-infinite behavior and eliminate the consequence of the boundary interacting with the region being considered for presentation. This requirement is evident in Fig.5.6 at $t = 5s$ where there exists an outflow of heat at $x = 1mm$. The outlet boundary condition in the simulation is set as outflow and would have influenced the temperature distribution upstream if the domain were truncated at $1mm$. It is important to provide an adequate amount of domain in semi-infinite problems to prevent the boundary interacting with the regions of interest and this is especially the case in this study where penetration depth in semi-infinite material is the motivation.

5.2.3 Stefan Problem using Propane in Porous Media

Equations 5.6-5.18 were developed by considering a volume averaging approach to incorporate the effects of the porous media in a manner identical to that which was used to develop Eqs.3.6-3.9. In this set of validations, the porosity is assumed to be $\chi = 0.32$ and the material properties are those of propane, Tab.5.2 and the grid utilized 6000 uniformly distributed nodes. Figures 5.7 and 5.8 describe the interface location and temperature distributions at various times.

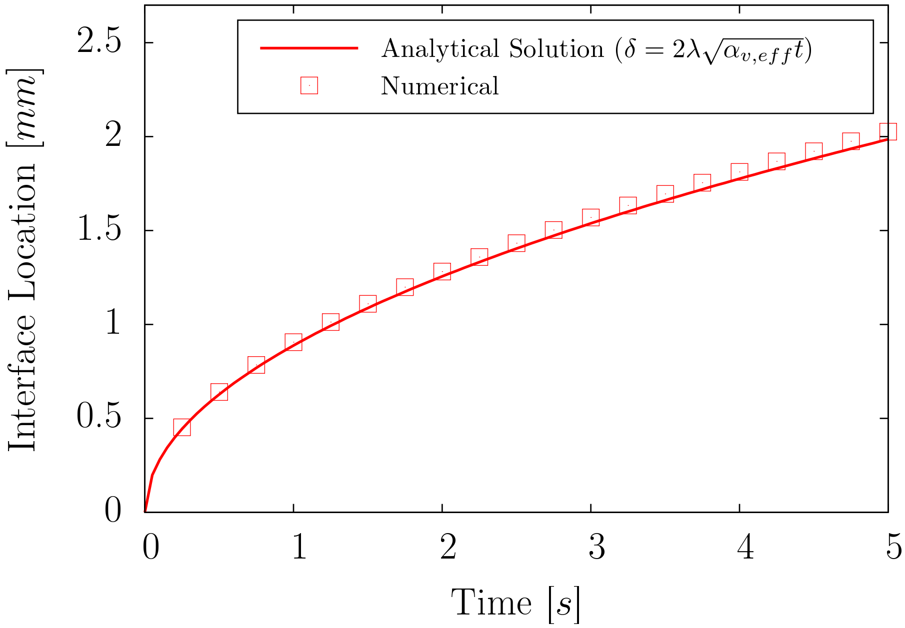

Figure 5.7: Interface location vs. time for liquid/vapor propane at $1.75MPa$ in porous media ($\chi = 0.32$) compared to the exact solution.

It is evident that the error is slightly more pronounced than in the cases without porous media. These discrepancies are attributed to the manner in which the VOF equation is modified to incorporate the effects of porosity. The standard solver, MULES, used to advect the interface does not contain such features by default and must be modified to include these effects. Since the accuracy of the solution is sensitive to time stepping and the interface velocity, incorporating a low porosity media results in an interface speed $1/\chi$ times faster than the Darcian velocity calculated by the PIMPLE solver.

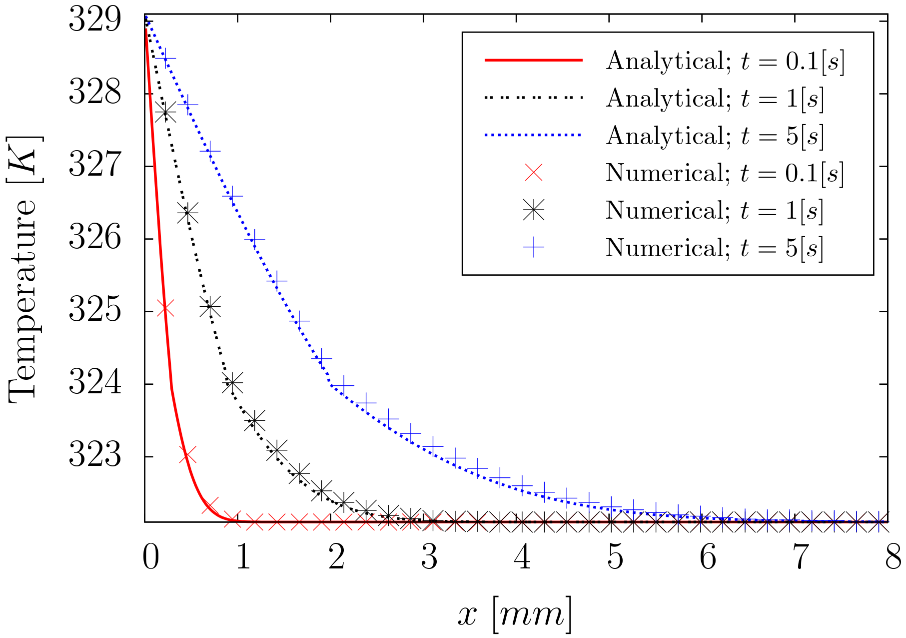

Figure 5.8: Temperature distributions for liquid/vapor propane at $1.75MPA$ in the vapor (left of discontinuity) and liquid phase (right of discontinuity) compared to the exact solution for a flow in porous media ($\chi = 0.32$).

5.3 Film Boiling

In order to assess the performance of the phase change solver in the presence buoyant and surface tension forces, a film boiling study was conducted and is presented here. The flow regimes typically found on a boiling curve consist of nucleate, transitional and film boiling where the former two require special care and attention as the absorbed liquid film at the boundary requires special care as the contact line along the boundary must be properly modeled with the consideration of heat transfer in the solid boundary. For work in this area, see [31, 33]. For simplicity and ease of comparison to analytical predictions of heat transfer coefficients, the simulation here is configured to perform in the film boiling regime where a vapor pocked separates the interface from the lower boundary which is fixed at a constant super-heat temperature. Berenson [49] developed an analytical model for the prediction of a mean heat transfer coefficient of an arbitrary fluid in the film boiling regime based on an instability analysis and assumptions regarding an average film thickness and vapor pocket/node separation distance, known as the most dangerous wavelength, Eq.5.19.

$$\lambda_d = 2\pi \left(\frac{3\sigma}{g_y(\rho_l - \rho_v)} \right)^{1/2} \tag{5.19}$$

The correlation predicts the mean Nusselt number normalized using a characteristic capillary length scale, $\lambda_o = (\sigma/(g_y(\rho_l - \rho_v)))^{1/2}$, differing from Eq.5.19 by a factor of $2\pi\sqrt{3}$.

$$\overline{Nu} = 0.425 \left[\frac{\rho_g(\rho_l - \rho_g)\vec{g}_y h_{fg}}{k_g \mu_g (T_{wall} - T_{sat})} \right]^{0.25} (\lambda_o)^{0.75} \tag{5.20}$$

Determining the mean Nusselt numerically consists of calculating the normal temperature gradient at each cell along the boundary, weighting by the local cell area and summing over the length of the boundary and finally dividing by the total boundary area and constant super-heat temperature.

$$\overline{Nu} = \frac{\lambda_o}{A_{wall}} \int_0^{\lambda_d/2} \frac{\partial T/\partial y}{(T_{wall} - T_{sat})} b dx \tag{5.21}$$

The boundary conditions for the simulation utilize the use of symmetry along the sides, atmospheric, fixed pressure at the outlet and a no slip condition at the lower, hot boundary at a constant super-heat temperature. Initially, the interface is set a finite distance from the heated boundary with a sinusoidal perturbation to help ease the solution into a quasi-steady state solution marked with periodic vapor pocket formation and pinch-off. The initial temperature is set to vary linearly in the y direction from the super-heat temperature to the saturation temperature at the interface. The liquid in the domain is initially saturated and remains constant due to the physics of phase change. Fig.5.9 depicts the configuration after the release of the first vapor bubble shortly after pinch-off.

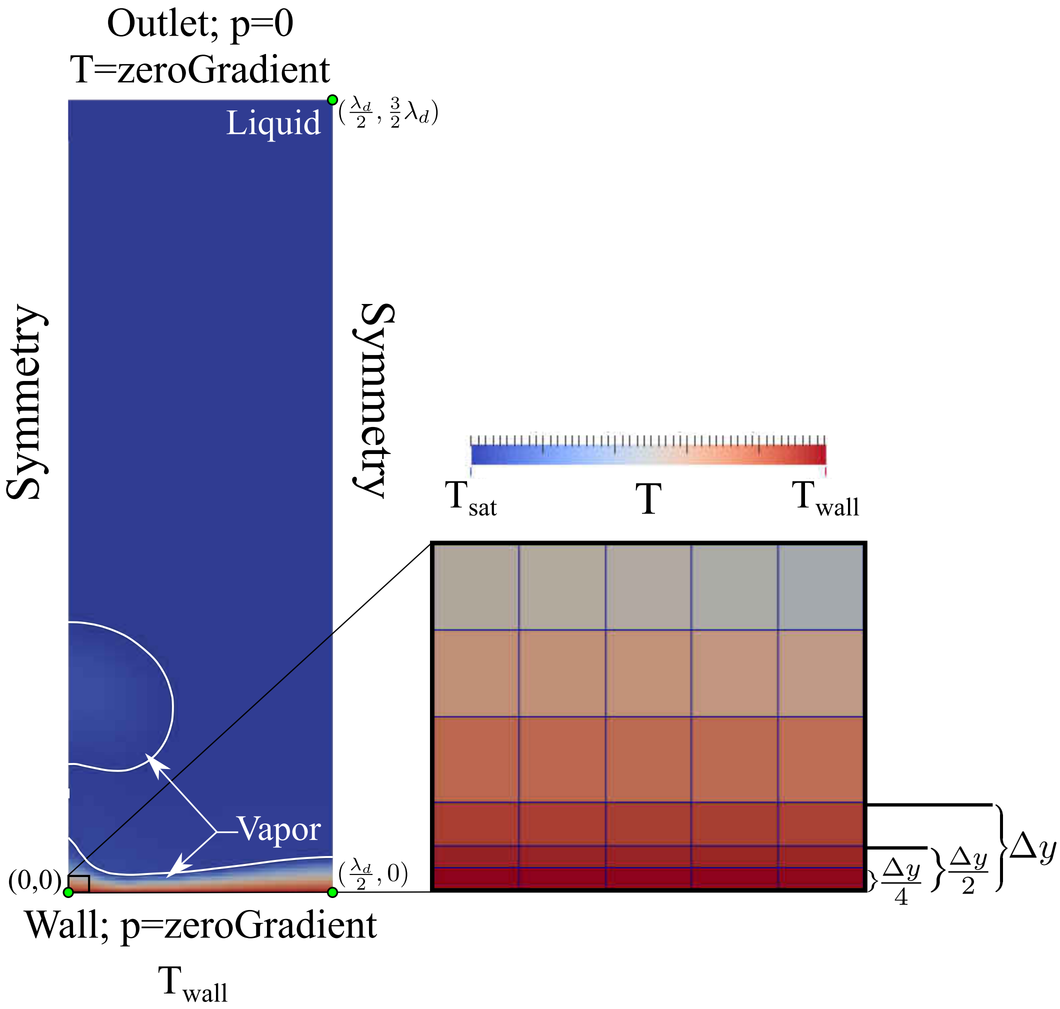

Figure 5.9: Film boiling schematic for 2D cases in this section. Two stages of grid refinement at the heated boundary occur in all cases presented in this section. The width of the domain is fixed at $\lambda_d/2$, half of the Rayleigh-Taylor most dangerous wavelength.

The mean Nusselt number varies periodically as the liquid/vapor interface drops close to the boundary in the presence of gravity and is then suddenly pushed away by the production of vapor at the interface. This vapor forms a viscous cushion over which the interface deforms to create the next vapor bubble which pinches off and rises out of the domain. In the cases where grid refinement is coarse, the viscous cushion separating the interface from the boundary is resolved by only a few cells. The no slip condition at the lower boundary should prevent the entry of interface cells adjacent to the boundary, however, when the boundary condition is poorly resolved by low grid resolution, interface cells are allowed to penetrate the region, and the ability of the simulation to stay within the film boiling regime is stifled as the source terms cannot exist in regions where the interface is present. This event prevents the formation of the viscous cushion of vapor over which the interface can glide. To mitigate this problem, the cells adjacent to the wall are split in two, in two stages, as illustrated in Fig.5.9.

The material properties for this set of simulations are chosen, consistent with [47], to be ideal as the heat and mechanical diffusivities are conducive to modeling with traditional VOF methodologies. The properties used in this study are presented in Tab.5.4.

Table 5.4: Bulk phase material properties for 2D and 3D film boiling validation.

	Property	Liquid	Vapor
ρ	Density ($\frac{kg}{m^3}$)	200	5
ν	Kinematic Viscosity ($\frac{m^2}{s}$)	0.5×10^{-3}	1×10^{-3}
C_P	Specific Heat ($\frac{J}{kgK}$)	400	200
k	Thermal Conductivity ($\frac{W}{mK}$)	40	1
h_{fg}	Heat of Vaporization ($\frac{J}{kg}$)	10000	
T_{sat}	Saturation Temperature (K)	500	
σ	Interfacial Tension ($\frac{mN}{m}$)	100	
λ_d	Most Dangerous Wavelength (m)	0.0787	
λ_o	Length scale (capillary) (m)	7.23×10^{-3}	
$\overline{Nu}$	Berenson Correlation [49] (1)	2.62	

5.3.1 Film Boiling 2D: Symmetry Plane ($\lambda_d/2$)

The tuning parameters such as C and $D\Delta t$ were chosen in ranges consistent with successful validations presented with the Stefan problems previously presented. A test of the overall performance of the solver is of primary interest, however, results will be shown for cases of varying C and the use of Kunklemann's [7] source term refinement where the interfacial transition region is stripped of source terms. A pictorial representation of the results at $0.2s$ intervals can be found in Fig.5.10.

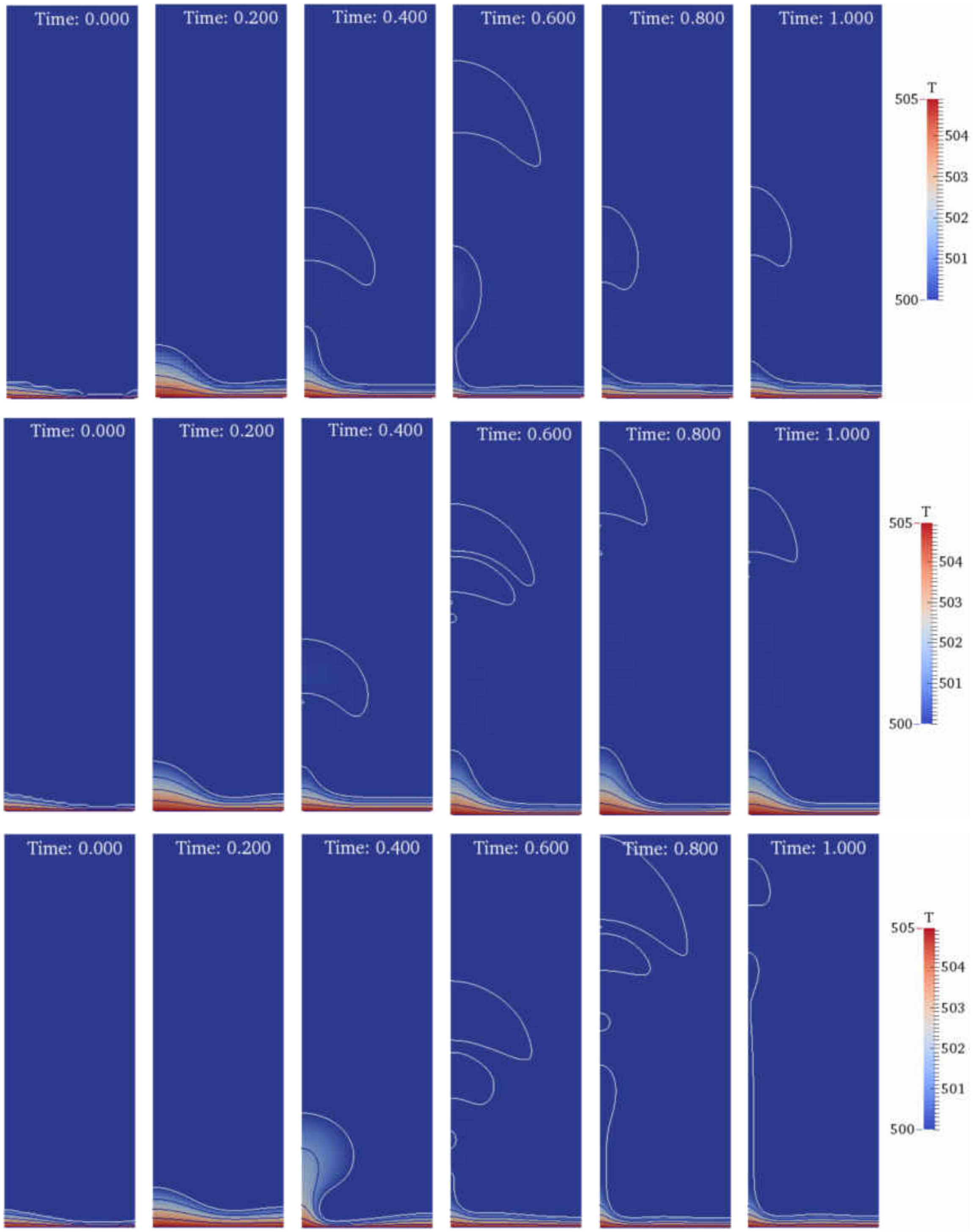

Figure 5.10: Film boiling results for 2D cases on uniform grids. $C = 1000000$ where source terms are removed from the interface consistent with [7]. Upper row: 32×96, Middle row: 64×192, Lower row: 128×384.

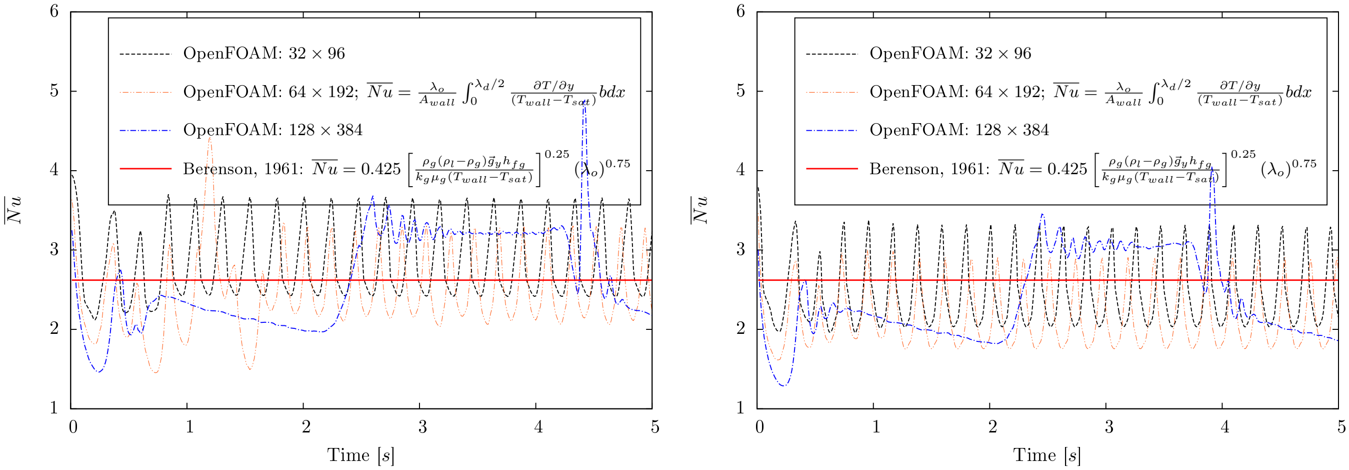

(a) $C = 10000$, source terms in the interface region.

(b) $C = 1000000$, source terms in the interface region.

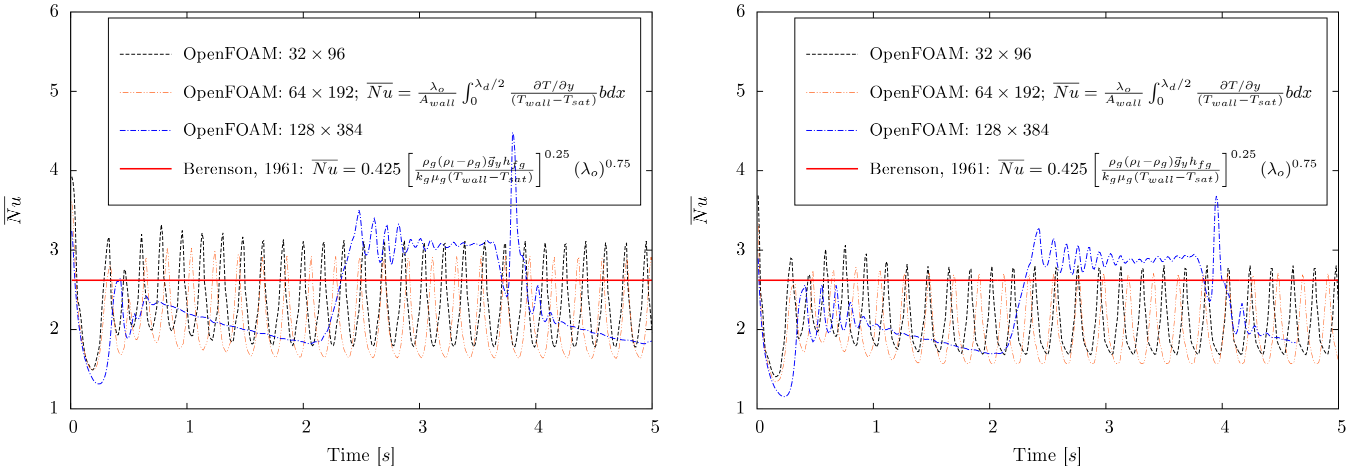

(c) $C = 10000$, source terms distributed by [7].

(d) $C = 1000000$, source terms distributed by [7].

Figure 5.11: Mean Nusselt vs. time for 2D film boiling. Upper row: source terms are present in the interfacial transition region. Bottom row: source terms are removed from the interface consistent with [7].

By comparison of the upper and lower rows of Fig.5.11, it is evident that the inclusion of Kunkelmann's Heaviside source term refinement (bottom row) tends towards a more consistent and uniform solution where the extremas of $\overline{Nu}$ are more uniform. For both of the above scenarios, it can be noted that as C increases, the system becomes more sensitive to deviations in the saturation temperature. As a result, when the interface progresses towards the heated boundary, the buffer layer formed by the vaporizing flow increases the separation distance between the heated boundary and the interface. This inherent increased system sensitivity with increasing values of C explains the net decrease in $\overline{Nu}$ with increasing separation distance. One interesting artifact of this film boiling study with the prescribed material properties is the grid convergence and how a quasi-steady vapor pocket formation and pinch-off transitions to the formation of a stable plume of vapor rising out of the domain connected by a narrow vapor column. It has been reported in the literature [6, 29] that grid convergence in many cases can lead to this vapor plume formation where the quasi-steady vapor pocket formation, as reported here, is a consequence of an unconverged grid. Though Welch *et al.* [47] were criticized for presenting $\overline{Nu}$ results for this fluid pair on an unconverged grid, the nonphysical quasi-steady vapor pocked formation and pinch-off allows for a comparison to an analytic expression for $\overline{Nu}$ that was developed based on the assumption that the formation of vapor bubbles occurs in a quasi-steady manner. This study serves to verify the aforementioned work for both the values of $\overline{Nu}$ as well as the nonphysical nature of the quasi-steady vapor pocket formation and pinch-off. The discussion of "physically realistic" is a bit premature for a 2D simulation as all of the out-of-plane surface tension forces are neglected. In other words, this "physical" stem of vapor that forms on a converged grid in 2D becomes increasingly difficult to maintain as the axisymmetric component of the surface tension force in 3D would favor the narrowing and pinching of this plume, tending towards a quasi steady vapor pocket formation. These cases are ideal in that only one λ_d is represented in the domain where the interaction of plumes may lead to instability, though, this is not always the case [39].

5.3.2 Film Boiling 2D: No Symmetry Plane (λ_d)

One case was run without of the use of a symmetry plane to demonstrate the influence of instabilities on the formation of a plume. When the symmetry plane is removed, instabilities and cross flows are allowed to destabilize the formation of a plue, resulting in a periodic shift from plume to vapor pocked/bubble formations. The grid was set to 256×384, the same resolution as the previous fine case, the Heaviside source term distribution was utilized [7] and $C = 1000000$. Figure 5.12 shows the result at a few time steps.

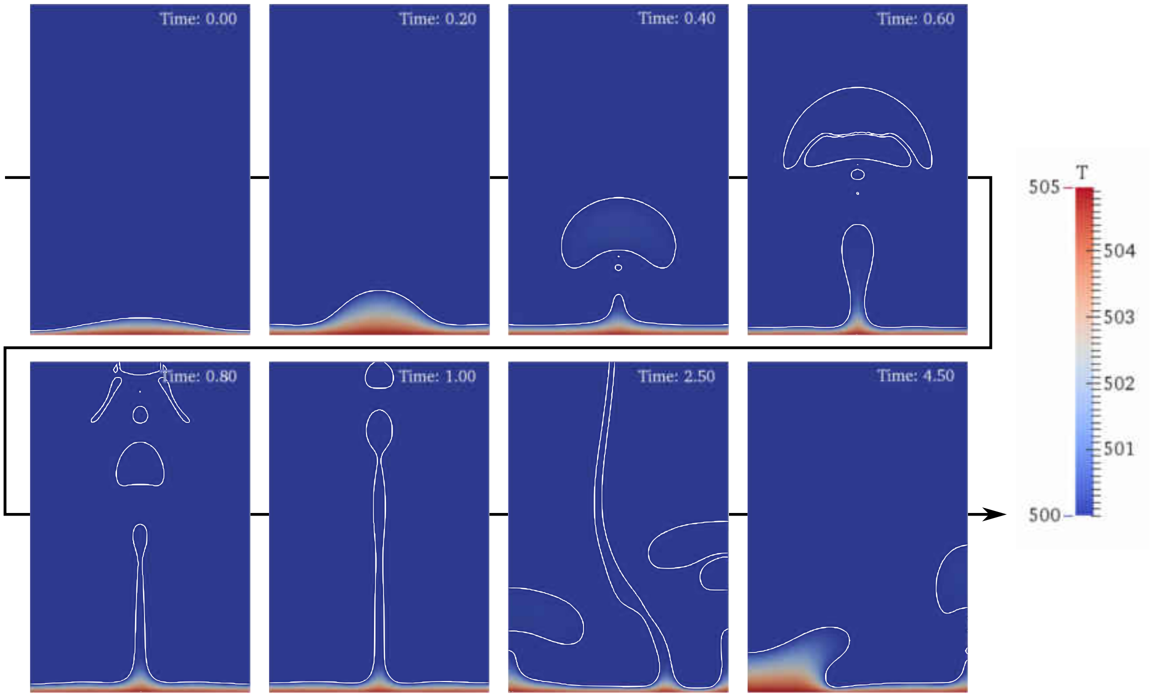

Figure 5.12: Film boiling results for a 2D case on a uniform grid without the use of a symmetry plane in the center of the domain. $C = 1000000$; Source terms distributed by [7] and 256×384 cells.

It is evident that there is a quasi steady formation of a plume consistent with the literature; however, the plume formation destabilizes at $t \approx 2s$ and transitions to the formation of vapor pockets and bubbles. Eventually the solution converges back on plume formations but is once again destabilized. Figure 5.13 shows that the results for this case don't vary much from those reported in Fig.5.11. The destabilization of the plume can be noted at $t \approx 2$ and $t \approx$ 4-4.5s where $\overline{Nu}$ increases rapidly resulting from portions of the interface reaching close to the boundary during bubble formation.

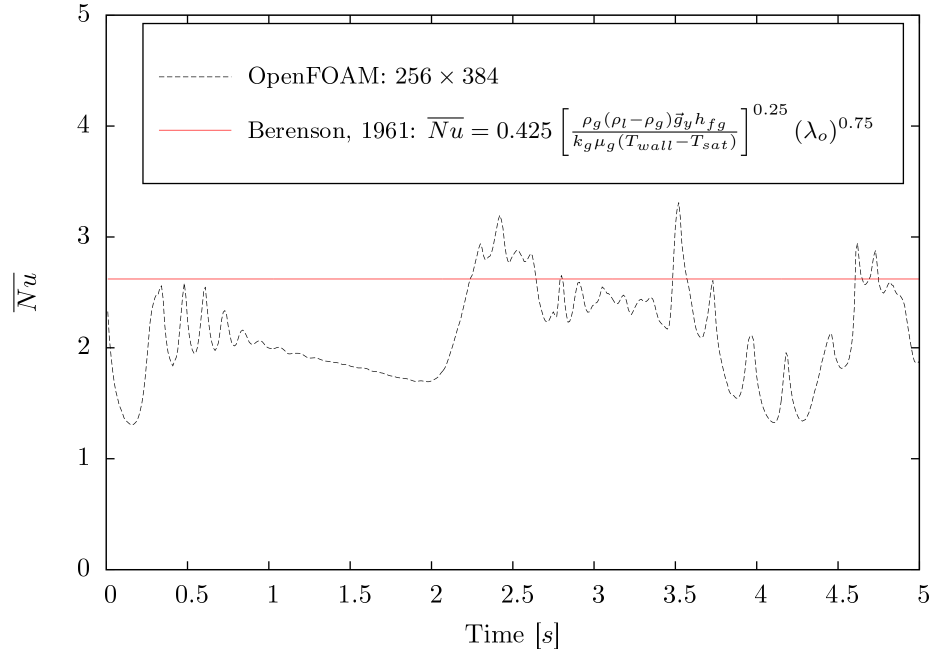

Figure 5.13: Mean Nusselt number for a 2D case on a uniform grid without the use of a symmetry plane in the center of the domain. Source terms distributed by [7] and 256×384 cells.

5.3.3 Film Boiling 3D

This section presents the results for a 3D study utilizing parameters consistent with the 2D cases discussed above. The domain is initialized to have dimensions of $2\lambda_d$ in all three coordinate directions with initial interfacial perturbations set in a square pattern with λ_d separating nodes in the x and y direction. The grid is uniform and the wall boundary cells were split similar to the 2D cases with an excess temperature of $5K$ and an initial linear temperature distribution. The purpose of this study is to assess, for increasing mesh density, whether or not the same observations can be made in the full 3D cases when compared to the 2D cases, Fig.5.14-5.16.

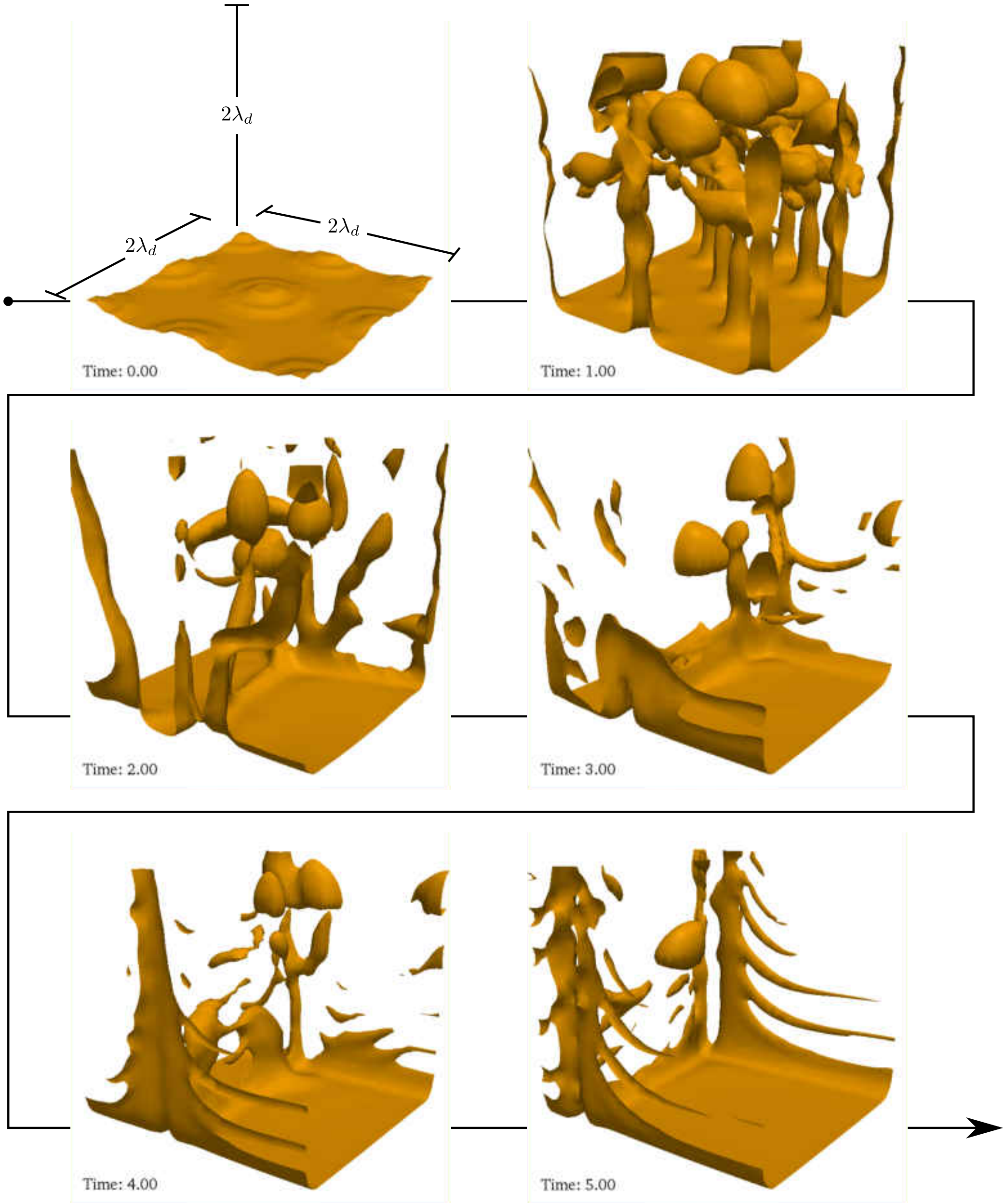

Figure 5.14: Film boiling results for 3D cases on a uniform grid of 40^3 cells, $C = 1 \times 10^6$ and where source terms are removed from the interface consistent with [7].

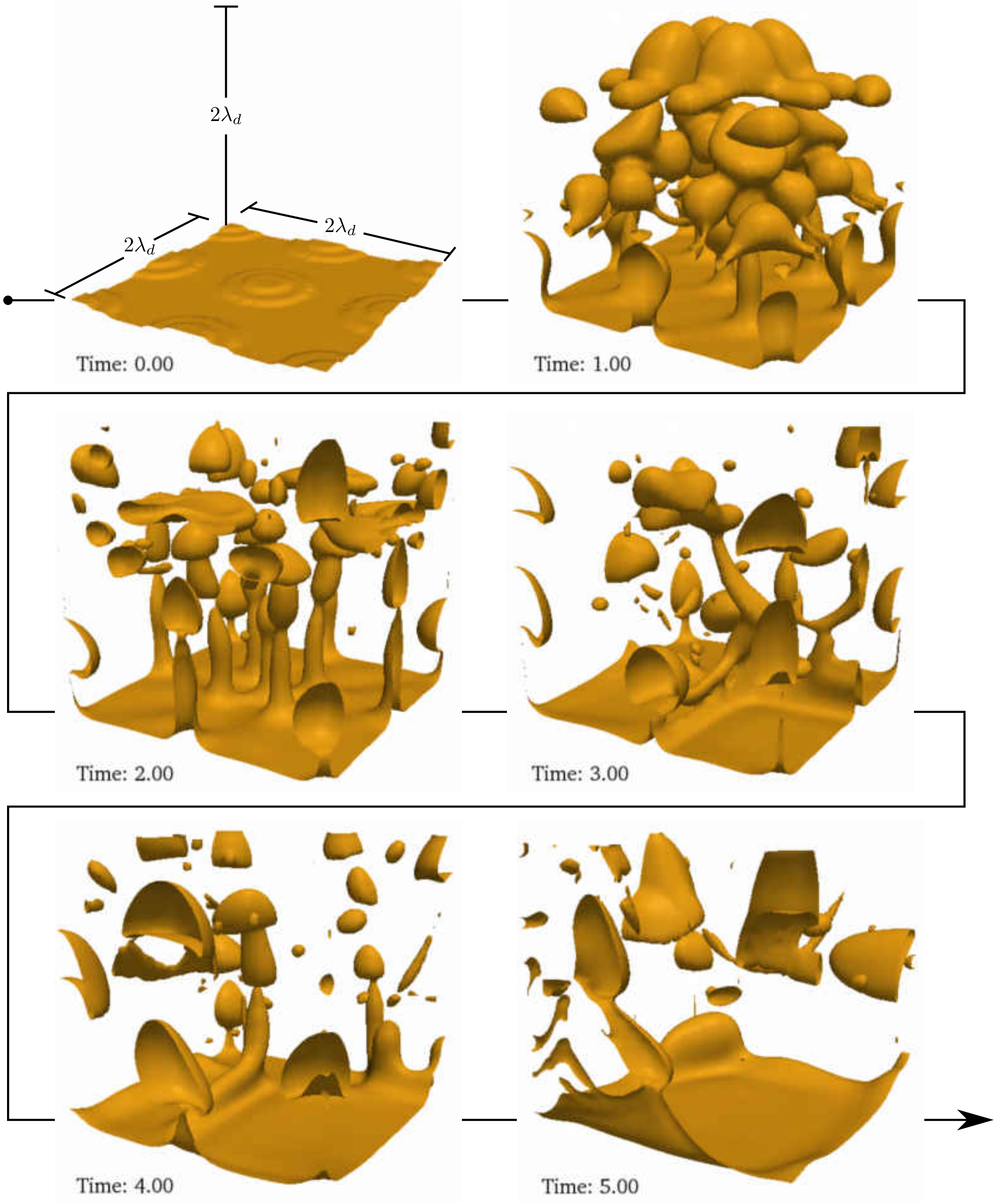

Figure 5.15: Film boiling results for 3D cases on a uniform grid of 70^3 cells, $C = 1 \times 10^6$ and where source terms are removed from the interface consistent with [7].

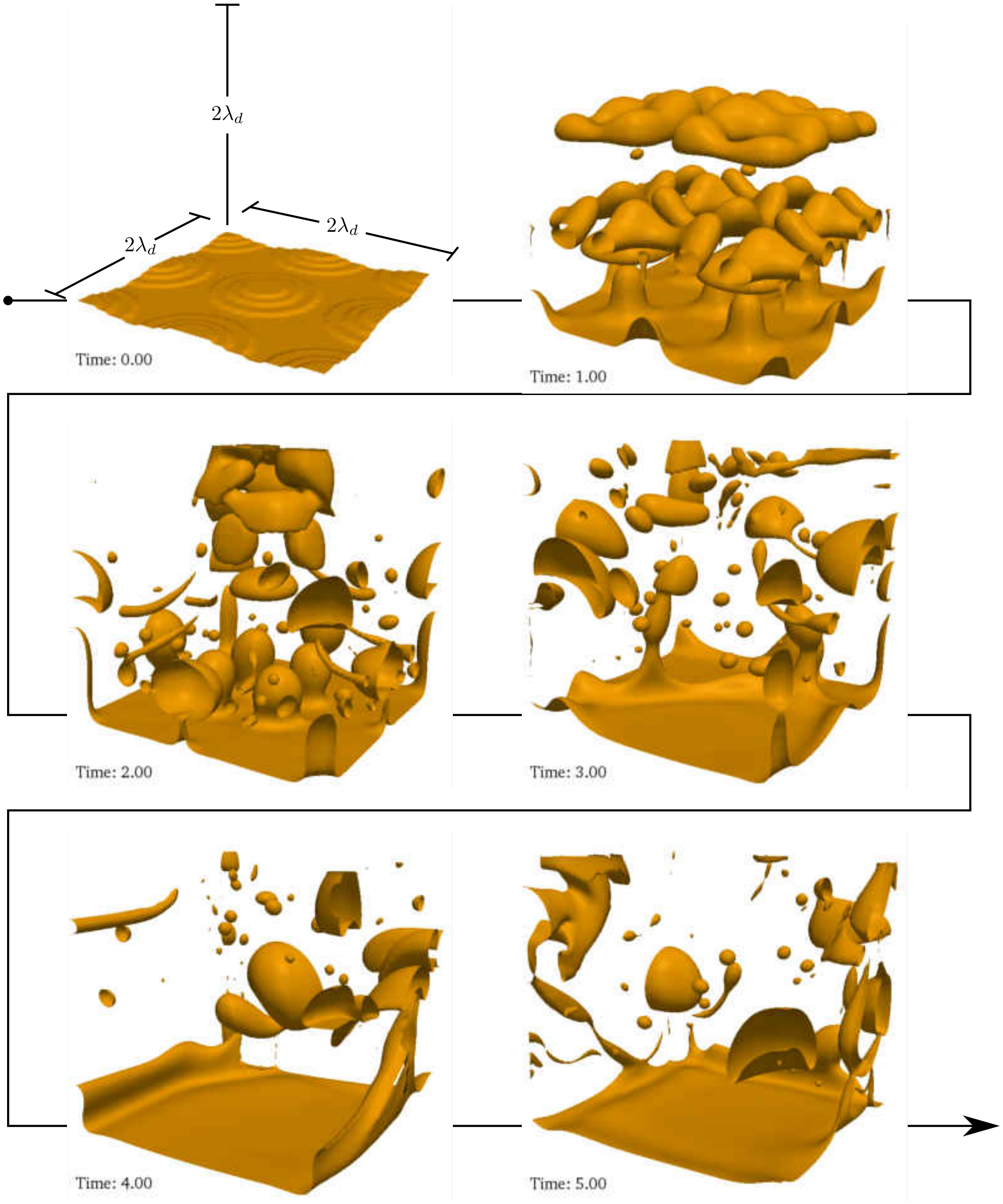

Figure 5.16: Film boiling results for 3D cases on a uniform grid of 100^3 cells, $C = 1 \times 10^6$ and where source terms are removed from the interface consistent with [7].

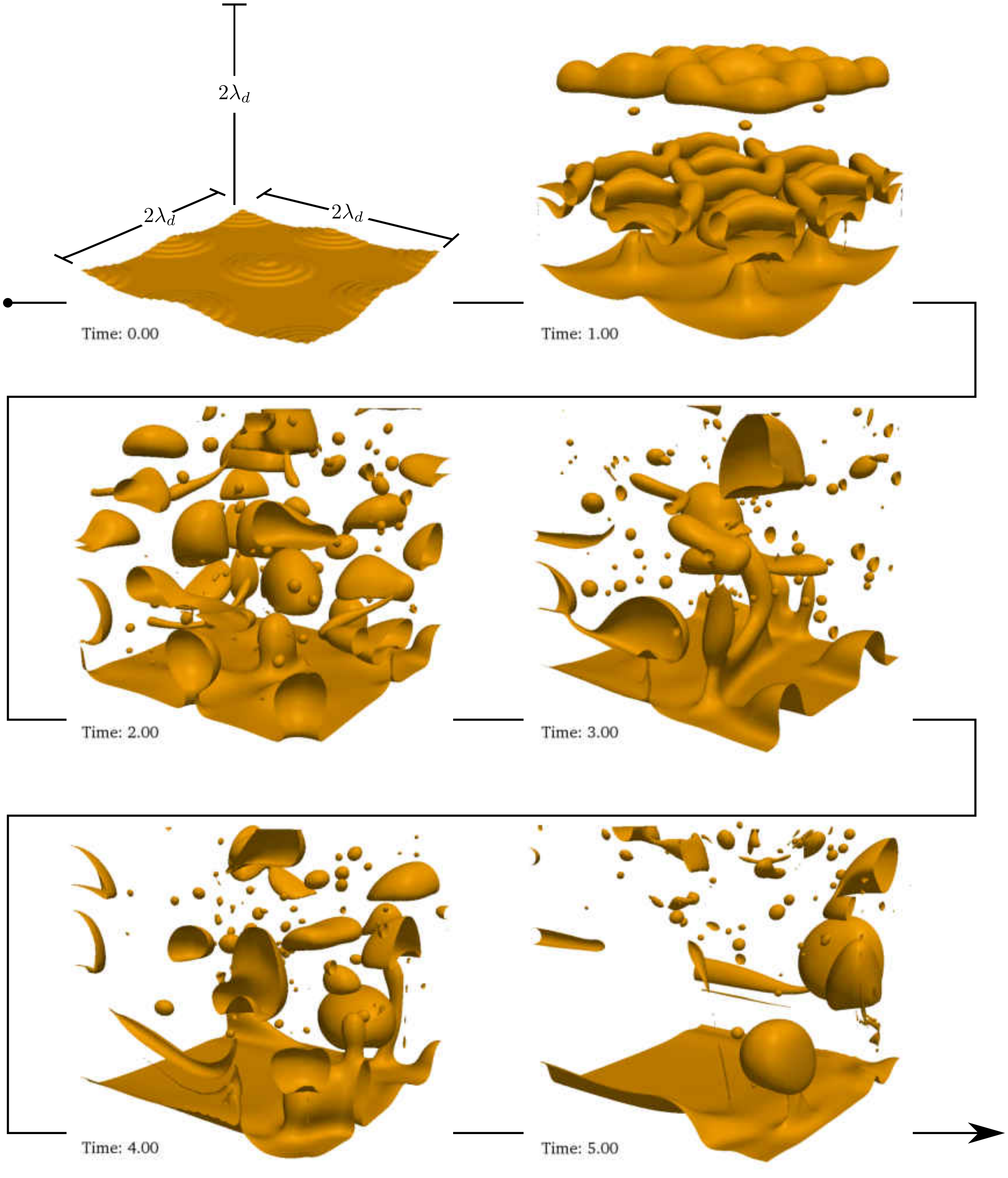

Figure 5.17: Film boiling results for 3D cases on a uniform grid of 130^3 cells, $C = 1 \times 10^6$ and where source terms are removed from the interface consistent with [7].

The figures above show time steps at $1s$ intervals of an isoplane drawn through an interpolated α field at $\alpha = 0.5$. The inclusion of the out-of-plane surface tension force acts to inhibit the formation of long plumes reaching the top of the domain that can be seen in the final pane of Fig.5.10 and also in Fig.5.12. Instead, the formation of plumes initializes while the cross flow currents in the domain are low. The pinch-off location occurs at a shorter distance as well, likely attributed to the out of plane surface tension force. The semi-stable plumes merge to the center of the domain at $t = 2.0s$ in Figs.5.14-5.17 due to the buoyant and surface tension forces. The plume merger then transitions to the formation of thin vapor films connected to rolling ligaments oriented horizontally. These bubbles/ligaments can be seen along the edge of the domain at $t = 3.0s$ in Figs.5.14 and 5.15.

As evidenced by the simulation results, the material properties and excess temperature for this simulation result in the formation of plumes, $t = 1.0s$ in Fig.5.14 and $t = 2.0s$ in Fig.5.15, however, the interaction with surrounding vapor jets and bubbles induce the instabilities leading to pinch-off. It can also be shown that there are similarities between the two studies where vapor pocket formation is favored and is most stable at the slip boundaries where the α boundary condition is maintained at `zeroGradient`. As a vapor jet or bubble makes contact with one of these boundaries, they tend to get stuck as the α contact angle adjusts, preventing migration away from the interface. This phenomenon can be seen as the formation of vapor pockets at $5.0s$ in Figs.5.14-5.17 occur primarily at the boundaries. In order to mitigate this, additional domain must be added to eliminate the effects of the boundaries on vapor pocket formation near the center of the domain [39].

The mean Nusselt numbers for the 3D film boiling cases (Fig.5.18) illustrate good agreement with Berenson's correlation, however, after about $2.0s$, $\overline{Nu}$ begins to decrease. This is a result of the plume and bubble formation occurring along the boundary in vertical sheets where the center of the domain is more or less stable with the absence of vapor pockets that would increase $\overline{Nu}$.

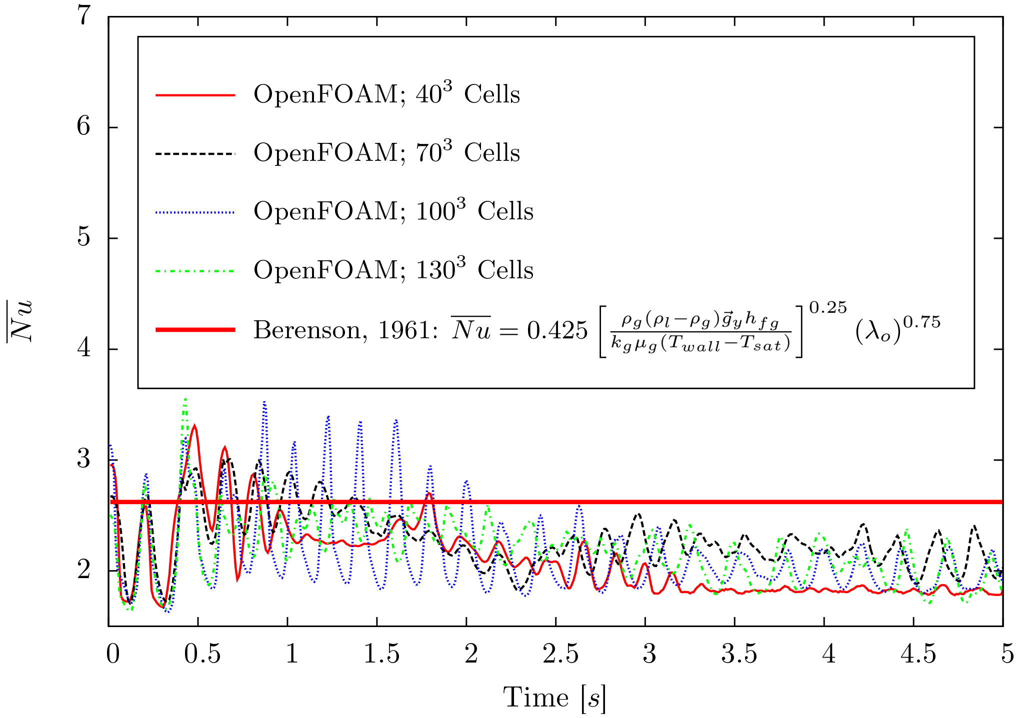

Figure 5.18: Mean Nusselt numbers for 3D Film boiling cases of increasing grid density. See Figs.5.14-5.16

The following section describes introduces the focus of this study where phase change will be occurring in porous media, lengths are on the order of $meters$ and the simulation times scales are on the order of days.

CHAPTER 6: PAY ZONE SIMULATION

This section is dedicated to the formulation of the phase change simulation used to predict penetration depths of saturated liquid propane at $1.75MPa$ in porous media of porosity, $\chi = 0.32$, and a range of permeabilities. Using the Stefan problems from the validations above in a similar manner, the parameters were chosen for stability and accuracy. The heat transfer processes involves the use of electromagnetic heating and solvents to aid in the mobilization of the bitumen for its efficient extraction from the pay zone. It should also be noted that in the T-P range specified, $\partial T_{sat}/\partial P \approx 0.03K/kPa$ and is therefore assumed to be constant as pressure gradients rarely exceed $10kPa$ for most cases.

The heat generation in the domain is an approximation of the heat generated by the use of a low frequency antenna, resulting in a volumetric heat source with a spatial distribution decreasing away from the well bore inlet. The volumetric heat source emitted by the antenna is approximated as an exponential function decaying in the radial direction from the well [50]. An initial profile is assumed in the solver and a correction factor is calculated to ensure the net heat rate delivered to the domain is equal to the power supplied to the antenna generating the RF energy. The expression relating the power of the antenna (W/m) to the heat generation in the domain is as follows

$$\dot{q}_{antenna} L = \frac{\iiint \Gamma \dot{q}_{heat} dV}{\iiint dV} = \frac{\iiint \Gamma e^{-\left(\frac{r-r_o}{l'}\right)} dV}{\iiint dV} \tag{6.1}$$

where $\dot{q}_{antenna}$ is the power per unit length of the antenna, L is the length of the well section under consideration, $\dot{q}_{heat}$ is the volumetric heat generation rate in the simulation domain, r_o is the radius of the desiccation zone assumed to be the radius of the well bore, l' is a characteristic length taken to be $1m$ for convenience. It should be noted that longer length scales should be used for low frequency electromagnetic heating. Γ is a correction factor calculated at runtime to ensure the heat generated per unit time is equal to the power supplied to the antenna.

$$\Gamma = \frac{\dot{q}_{antenna} L}{\frac{\iiint \dot{q}_{heat} dV}{\iiint dV}} \tag{6.2}$$

Since the focus of this study is to determine the acceptable flow rates supplied to the domain, the problem formulation will consist of testing a series of volume flow rates against the conditions provided such as the permeability and the antenna power.

To better understand the physical processes involved, various cases will be studied to separate the physical processes present in the vaporizing flow. The contribution of gravity, the addition of thermal energy and the transition of the fluid from the free flow regions to porous media will be considered. The configurations will include:

- Porous media without gravity
- porous media without gravity
- Porous media and free flow transitions with gravity

By eliminating gravity in the first case, the liquid is allowed to permeate through the pay zone where the increasing temperature is acts to vaporize the progressing liquid/vapor front. The second configuration is streamlined to allow for running test cases at a high throughput for mapping anticipated flow regimes where the solvent may over saturate the bitumen pay zone. The following section introduces the first configuration, porous media in the absence of gravity. Finally adding the transition from free flow to porous media in the presence of gravity provides useful information regarding initial transient flow behavior in the vicinity of the wellbore porous media boundary.

6.1 Pay Zone Simulation: No Gravity in Porous Media

This case study was conducted in order to investigate the combined effects of heat transfer and fluid mechanics without the interaction of the fluid with the free flow/porous media interface or gravity. Excluding the effects of gravity and porous media/free flow interaction allows for the determination of the case configurations to follow and reduces the computational expense. The computational domain, Fig.6.1, illustrates the section of the well bore and its surroundings utilized to study the penetration depth of liquid propane in porous media.

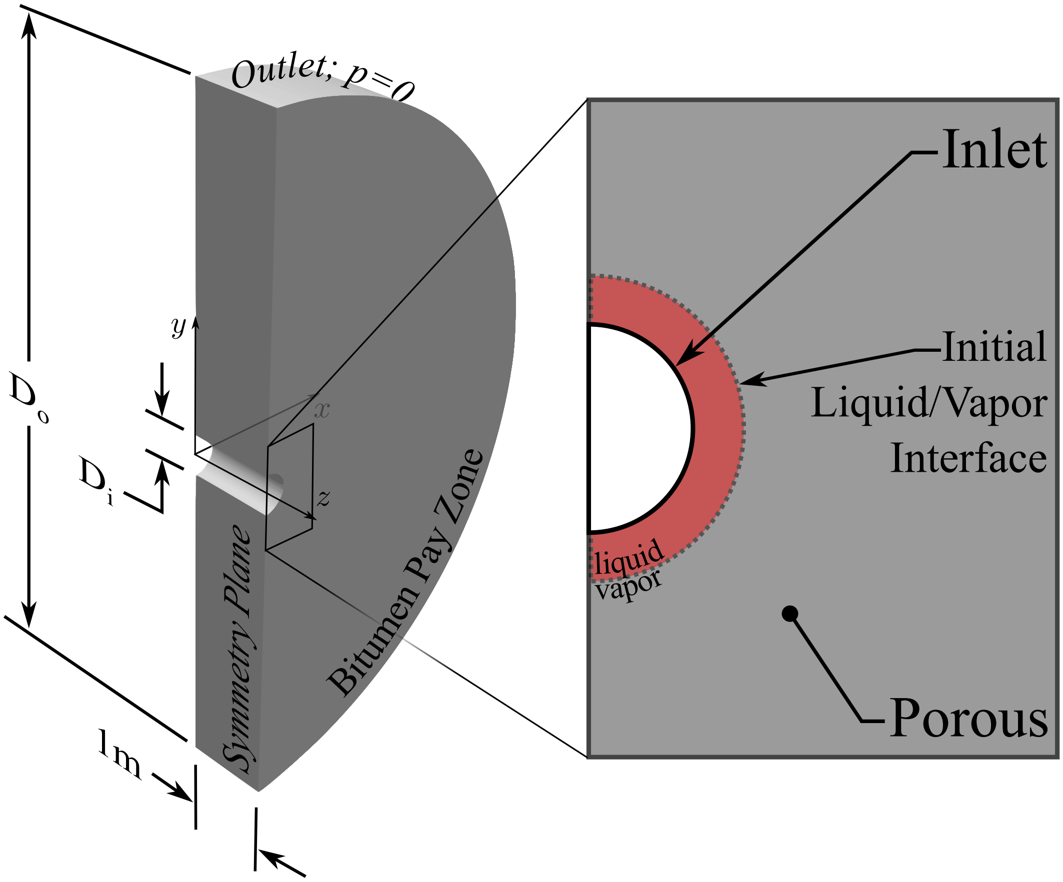

Figure 6.1: Computational domain containing bitumen pay zone for the cases without gravity or transitions from free flow to porous media regions of the domain.

The depth of the domain in the z direction is set at $1m$ for all cases to simplify the analysis. The relevant parameters for this case are defined as $D_i = 0.483m$, $D_o = 8m$, $\chi = 0.32$ and $\Pi = 3000mD$.

The goal for this case study is to determine the effect of the mass flow rate on the penetration depth in the presence of a constant heat rate. This assumption results fundamentally in a 1D problem where liquid entering the domain at the saturation temperature is allowed to permeate into the infinite surroundings which are also initially at the saturation temperature. Though axial symmetry could be utilized here, a 2D formulation is preferred as the addition of gravity will follow in later sections. The mass flow rates utilized are presented in Tab.6.1.

Table 6.1: Model mass flow rates for cases I-III without gravity.

	Case I	Case II	Case III
$\dot{m}(\frac{kg}{s})$	1.93×10^{-4}	3.86×10^{-4}	5.79×10^{-4}

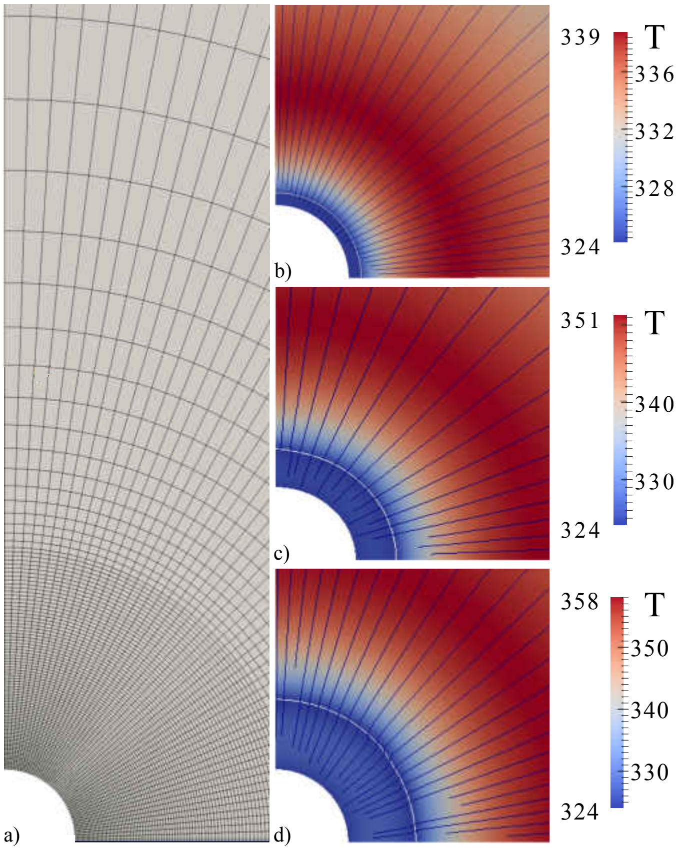

Figure 6.2: a). Computational grid. b)-d) 2D color plots for temperature, volume fraction (white line along interface where $\alpha = 0.5$) and rendered stream lines (dark blue lines extending radially from the well) for cases I-III (b-d respectively) at the maximum penetration depth.

A simulation time of $200 \times 10^3 s$ was allotted to capture the progression of the interface through the semi-infinite medium. The domain is comprised of 10000 structured hexahedra extending radially and circumferentially away from the injector well with a dense concentration focused around the liquid propane inlet (Fig.6.2a). Due to the relatively large heat of vaporization and low heating and mass flow rates, small changes occur over long time scales. As a result, the time steps were allowed to reach 1-$5s$ per iteration where little changes in the steady penetration depth occurred with increased temporal resolution. For the given time steps and spatial grid resolution, a value for C was chosen to be $1 \times 10^6 kg/(m^2 sK)$.

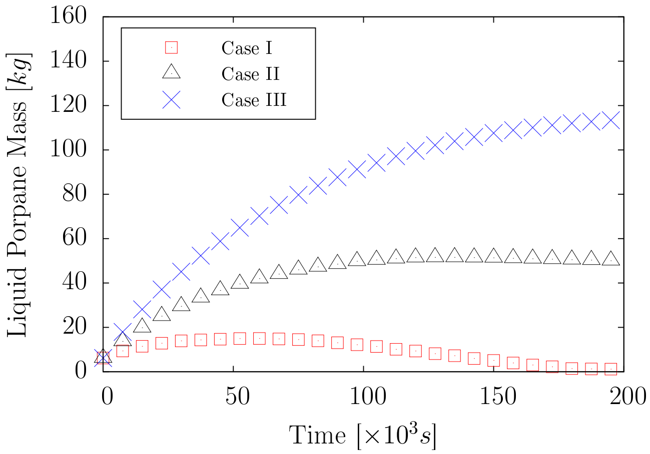

Figure 6.3: Time histories of liquid mass content contained within the computational domain for different mass flow rates in cases I-III without gravity.

Figure 6.3 displays the liquid propane mass time history for each of the three cases. It is evident that as the mass flow rate increases from case I-III, the penetration depth increases. For all three cases, the liquid interface penetrates the fastest initially and eventually slows to a stop where the increase in temperature caused by the RF heating begins to inhibit the further progression of the interface through vaporization. Not only does the liquid encounter the ever increasing temperatures due to the heating, but mass continuity dictates the decaying rate of progression away from the well even in the absence of phase change.

Another contributing factor to the regression of the interface is the heat generation that occurs in the liquid phase of the propane. Since the physics of phase change are confined to the interface of this immiscible two fluid solver, the heat generated in the liquid phase conducts to the interface and further increases the rate of phase change and consequently, the regression of the interface towards the well. The temperature distribution of the pay zone at the *stagnation* point of the moving interface for each case can be seen in Fig.6.4 as well as in Fig.6.2 where the line plots (Fig.6.4) are taken along $(x, y = 0)$. The temperature profiles are shown to increase in magnitude from case I-III. This results from the increased time required to generate the heat required to stop the progression of the interface for the increasing mass flow rate from case I-III. Note the temperature (the red, thicker lines) at the location where the (blue, thinner lines) liquid propane volume fraction curves intersect for each case. This location is the liquid/vapor interface. Here, the temperature sharply dips down to the saturation temperature as prescribed by Eq.2.5. The shape of the temperature profiles reflects the heat generation distribution added by the antenna.

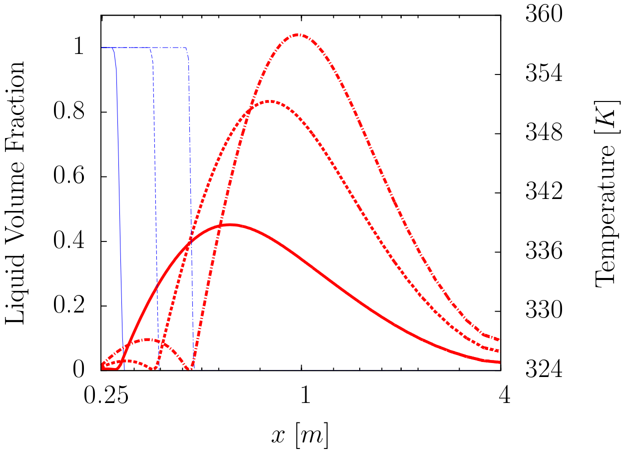

Figure 6.4: Volume fraction and temperature profiles along $x, y = 0$ at the times corresponding to the maximum liquid penetration depth measured from the injector will for cases I-III (solid $-$, dashed - -, and dash-dot -·- respectively). Thinner blue lines to the left correspond to volume fraction of liquid propane and larger red lines to right correspond to temperature.)

Since all of the thermal fields are assumed to be saturated initially, the interface progresses through the domain with a minimal amount of phase change. There are three distinct regimes that describe the progression of the interface through the porous media. They are, 1) forward propagating penetration by the liquid/vapor interface, 2) an equilibrium regime where the rise in temperature caused by the antenna provides enough thermal energy to slow and stop the interface motion and finally, 3) the regression of the liquid/vapor interface back to the well bore as the temperature continues to increase. The functional dependence of the time at which the interface begins to slow and regress is complex and depends on numerous factors, namely the initial temperature of the domain and the liquid entering from the well and the mass flow rate. Any one of these parameters can be manipulated to ensure complete liquid vaporization, however, the targeted parameter, such as a minimum mass flow rate, may not be satisfied as a result. This case serves an integral role in determining the feasible starting points for the cases to follow.

6.2 Pay Zone Simulation: Gravity in Porous Media Regions

This case study was conducted in order to investigate the combined effects of heat transfer, fluid mechanics and gravity without the interaction of the fluid with the free flow/porous media interface. Excluding the effects of porous media/free flow interaction allows for the determination of a transitional locus where the case configuration moves from full vaporization to partial/incomplete vaporization, at a reduced computational expense. The computational domain, Fig.6.5, illustrates the section of the well bore and its surroundings utilized to determine the transition between the aforementioned regimes.

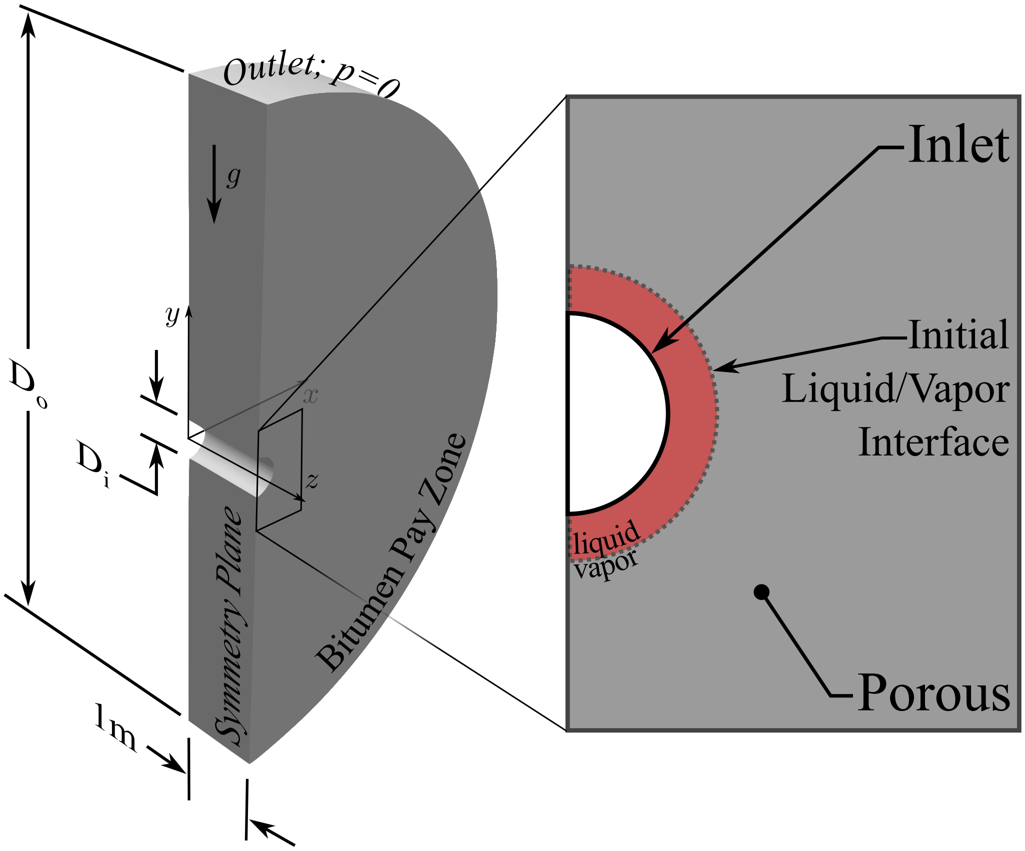

Figure 6.5: Computational domain containing bitumen pay zone for the cases with gravity and without transitions from free flow to porous media regions of the domain.

This case is identical to the previous case with a few exceptions. The inclusion of gravity is considered as well as a decrease in D_o from $8m$ to $2m$ and a grid resolution of 11250 cells distributed primarily around the inlet of the wellbore. The inlet diameter, D_i, also decreased from $0.483m$ to $0.248m$. The solvent utilized here is also propane at $1.75MPa$, Tab.5.2.

The series of cases studied here references the results for the previous configuration. The current configuration recognizes that for the low mass flow rate of $\approx 1 \times 10^{-4}$ in the previous case, the time scale for full vaporization required nearly $2 \times 10^5 s$. In order to increase temporal resolution of the dynamics associated with a liquid/vapor interface deforming in the presence of gravity, the minimum mass flow rate is increased an order of magnitude. The range of solvent delivery rates, heat rates and permeabilities considered in this case configuration are presented in Tab.6.2.

Table 6.2: Case parameters considered for the flow of saturated propane at $1.75MPa$ into a porous domain of porosity, $\chi = 0.32$, in the presence of gravity.

$\dot{q}[kW]$	$\Pi[mD]$	$\dot{m}[kg/s]$
1-10	25-6000	1.15×10^{-3}-5.76×10^{-3}

For any of the cases presented in this section, a low heat and solvent delivery rate were selected initially as the constant parameters and the permeability was the varied until a qualitative transition from full vaporization to partial/incomplete vaporization was observed. The permeability was selected at the low end of the range described in Tab.6.2 and was gradually increased as the low permeability values promote stable liquid penetration into the domain. The fluid and interface Courant numbers, as a result, were lower than the cases with high permeabilities for the same flow rate and heat rate yielding lower run times. Once two values of the permeability bisect the transition locus between full and partial/incomplete vaporization, the point was saved. This process is repeated for the same heat rate and for increasing solvent delivery rates. Once the locus points for a given heat rate could produce a line or curve spanning a sufficient permeability and solvent delivery rate range, the heat rate was increased, repeating the process. The final result was a series of curves that were used to construct a surface in 3D to identify the division between regimes undergoing full and partial/incomplete vaporization. The assessment of whether the flow was considered fully vaporized was based primarily on the mass content exiting the domain. If all of the mass exiting the domain during the simulation was entirely vapor, and continued to remain vapor, the configuration was considered to be vaporized. Now suppose the mass exiting the domain was full of unvaporized solvent, the configuration would be considered unvaporized. On the other hand, the flow may initially appear to be unvaporized, however, as time progresses within the time scale of the simulation, the temperature in the domain increases to the point where the progressing interface is stopped and the liquid mass changes rapidly vaporizes to the point where the configuration can be considered fully vaporized. For some cases the qualitative assessment is very difficult to make. For these instances, the domain mass vs. time is plotted and behavior of the resulting curve provides a more quantitative means of determining full vaporization. Equation 6.3 shows the method for calculating the liquid mass in the domain at various times. The mean temperature in the domain is also considered for these cases as vaporization results in a reduction in temperature due to latent cooling. This is in contrast to the increase in mean temperature caused by the RF heating. The expression for the mean temperature can be fond in Eq.6.3.

$$m = \iiint \rho_l \alpha dV; \;\; \overline{T} = \frac{\iiint TdV}{\iiint dV} \tag{6.3}$$

Figure 6.6 shows the transition from vaporized to partial/incomplete vaporization by changing the permeability from 100 to $50mD$, for a heat rate of $1.5kW$ and a flow rate of $0.00230kg/s$.

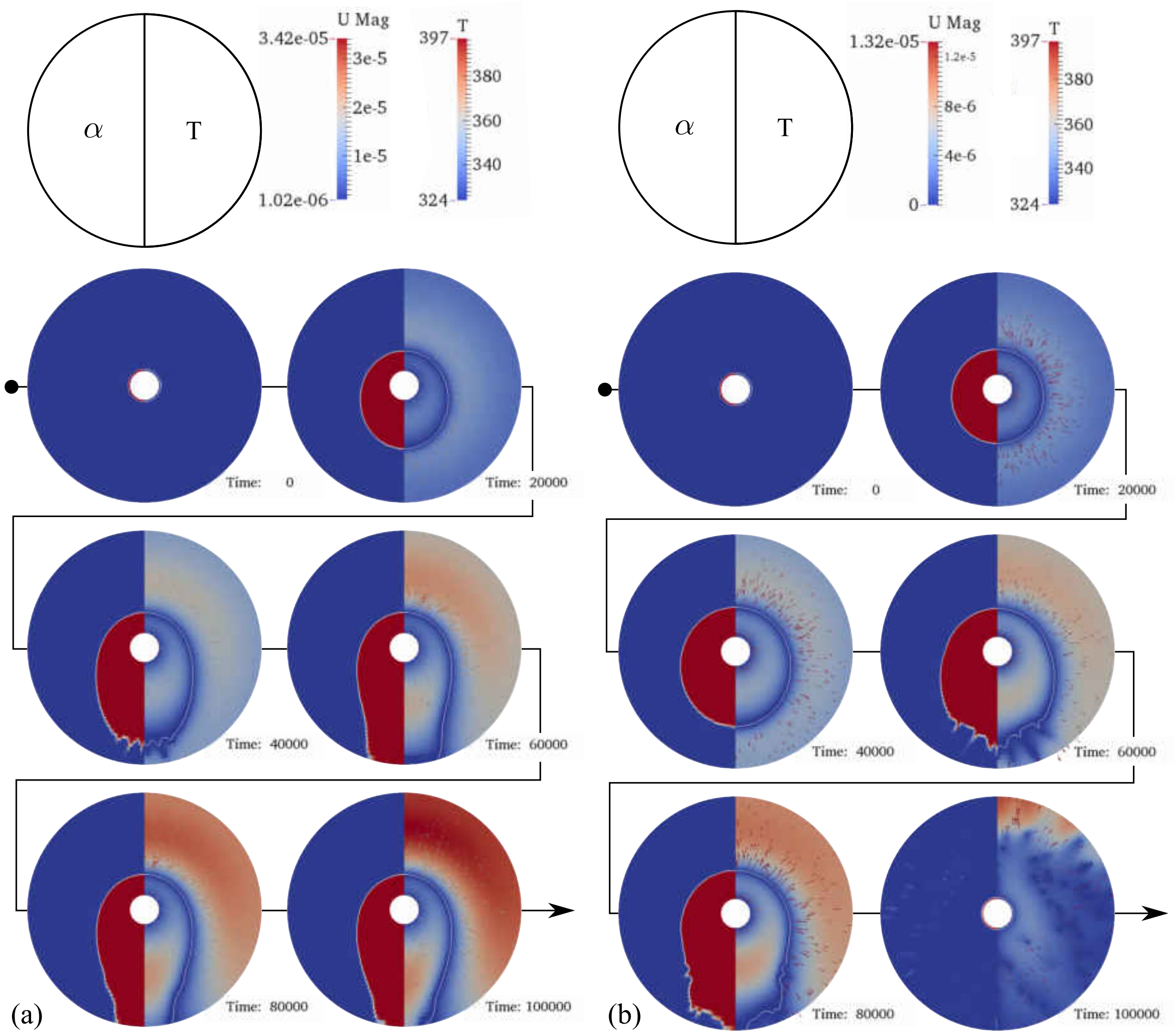

Figure 6.6: Color plots of volume fraction (left hemisphere → red: liquid; blue: vapor) and temperature (right hemisphere) for a mass flow rate of $0.00230 kg/s$ and a heat rate of $1.5 kW$. The liquid vapor interface is drawn by a solid white line and velocity vectors are superimposed over the plots. The results are presented at $20000 s$ intervals and show the progression of the interface in the presence of gravity and phase change resulting from the increase in temperature. The plot in (a) illustrates the progression of the interface out of the domain for a permeability of $100 mD$. The plots in (b), on the other hand, illustrate how for a slightly lower permeability of $50 mD$, the liquid mass vaporizes entirely prior to exiting the domain.

The line plots for the domain mass and mean temperature can be see in Fig.6.7.

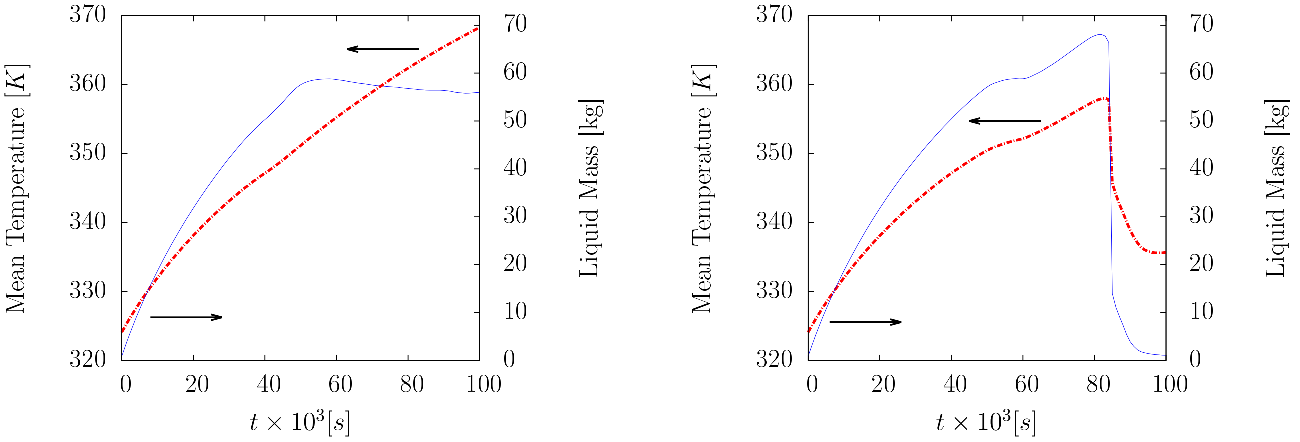

(a) $\dot{m} = 0.00230[kg/s]$; $\dot{q} = 1.5[kW]$; $\Pi = 100mD$

(b) $\dot{m} = 0.00230[kg/s]$; $\dot{q} = 1.5[kW]$; $\Pi = 50mD$

Figure 6.7: Domain volume averaged Temperature (-·-) and liquid mass content (—). The plot in (a) illustrates how the mass content in the domain decreases at about $50000s$ while the mean temperature continues to increase smoothly, indicating that large regions of high density liquid exits prior to vaporization. (b), on the other hand, illustrates a sharp decrease in liquid mass content accompanied by a corresponding decrease in mean temperature resulting from latent cooling during vaporization. For this lower permeability, the liquid fully vaporizes prior to exiting the domain.

It is evident that at $60000s$ in Fig.6.6, the width of the liquid region is greater for the case of $\Pi = 50mD$. This is a consequence of the greater flow resistance added by the porous media when compared to the gravitational forces. This contribution keeps the interface closer to the heated region near the wellbore and, as a result, the liquid mass has a sufficient amount of time to vaporize. The line plots in Fig.6.7 shows in a more quantitative manner how the mass content in the domain decreases as the liquid vaporizes. At about $50000s$ in Fig.6.7.(a), the mass content in the domain levels off as the liquid exits the domain. A subtle decrease can seen after this point as the increasing temperatures aid in vaporizing the liquid entering the domain. In Fig.6.7.(b), the same observation can be made at about the same time, however, the liquid mass rapidly vaporizes where the liquid mass drops suddenly along with the mean temperature due to the latent cooling.

Figure 6.8 shows the transition from vaporized to partial/incomplete vaporization by changing the permeability from 3000 to $2000mD$, for a heat rate of $5kW$ and a flow rate of $0.00115kg/s$.

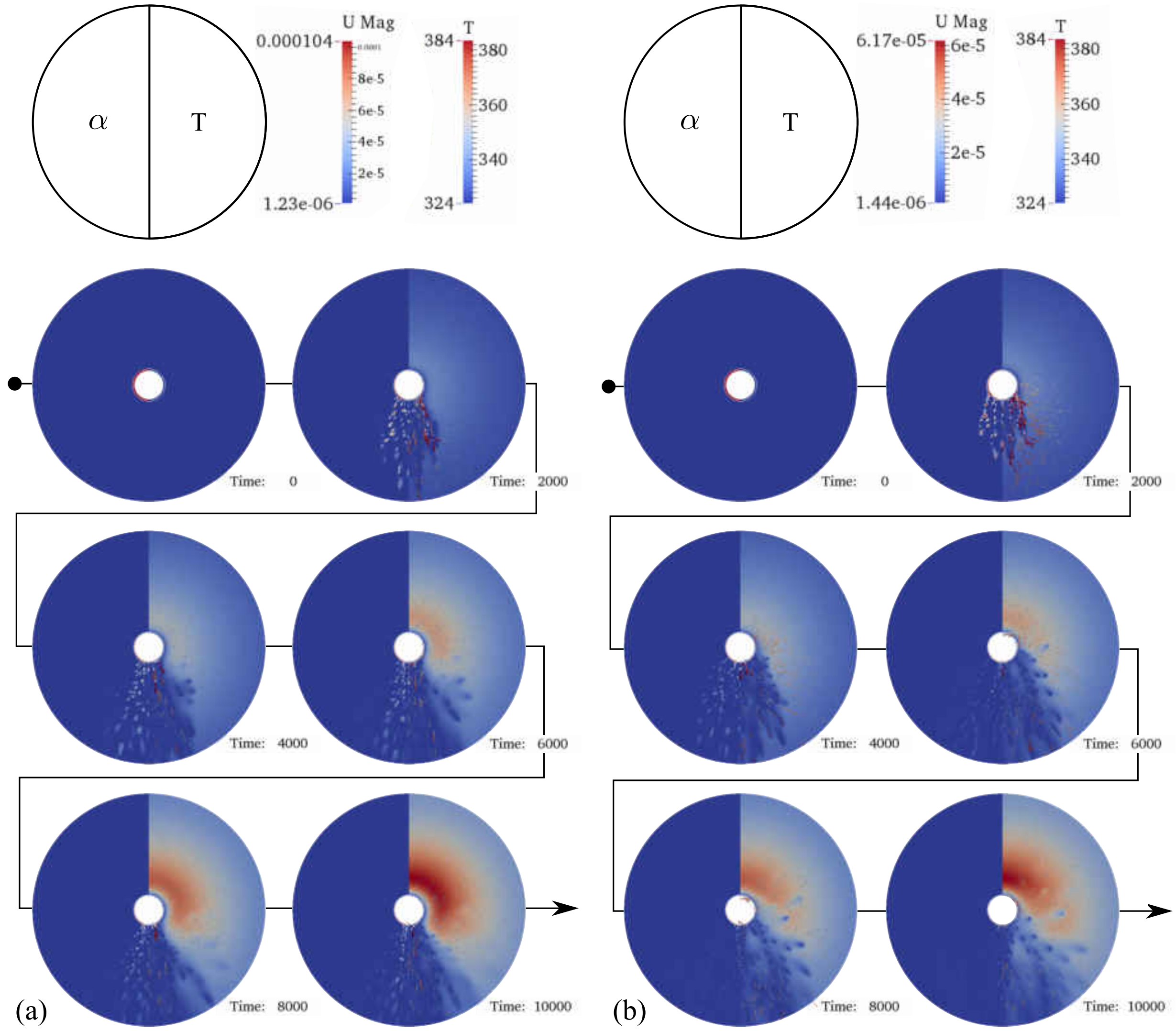

Figure 6.8: Color plots of volume fraction (left hemisphere → red: liquid; blue: vapor) and temperature (right hemisphere) for a mass flow rate of $0.00115[kg/s]$ and a heat rate of $5kW$. The liquid vapor interface is drawn by a solid white line and velocity vectors are superimposed over the plots. The results are presented at $10000s$ intervals and show the progression of the interface in the presence of gravity and phase change resulting from the increase in temperature. The plot in (a) illustrates the progression of the interface out of the domain for a permeability of $3000mD$. The plots in (b), on the other hand, illustrate how for a slightly lower permeability of $2000mD$, the liquid mass vaporizes entirely prior to exiting the domain.

The line plots for the domain mass and mean temperature can be see in Fig.6.9.

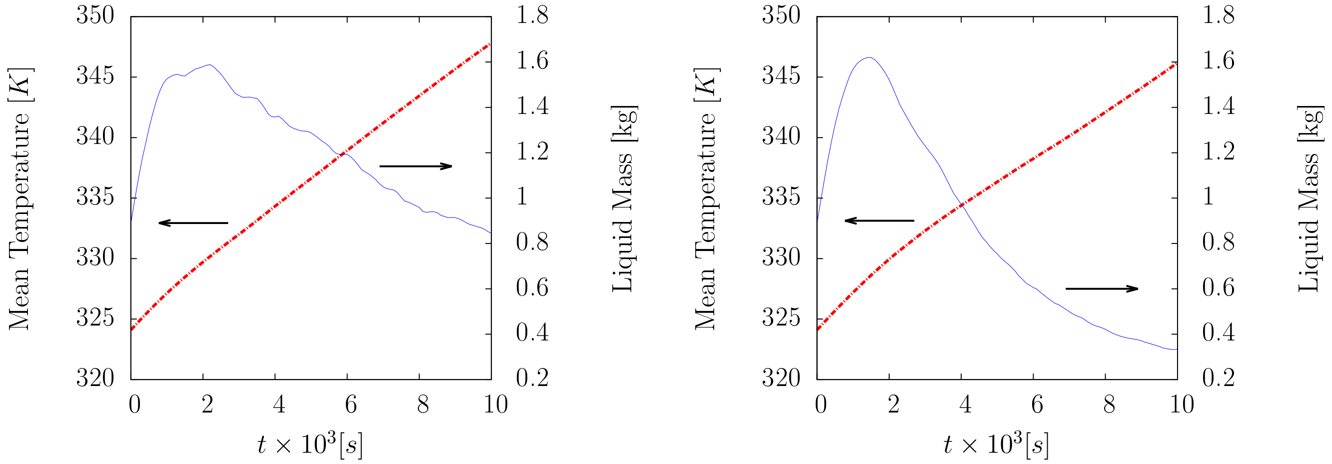

(a) $\dot{m} = 0.00115[kg/s]$; $\dot{q} = 5[kW]$; $\Pi = 3000mD$

(b) $\dot{m} = 0.00115[kg/s]$; $\dot{q} = 5[kW]$; $\Pi = 2000mD$

Figure 6.9: Domain volume averaged Temperature (-··-) and liquid mass content (—). The plot in (a) illustrates how the mass content in the domain decreases suddenly where the line plot looks rough, indicating liquid solvent exiting across the domain boundary. (b), on the other, hand illustrates a smooth descent to a lower value of mass at the end of the solution. For this lower permeability, the liquid fully vaporizes prior to exiting the domain. A drop in mean temperature can be observed between cases resulting from latent cooling.

It is evident from the color plots in Fig.6.8 that the difference in liquid mass exiting the domain is difficult to qualitatively assess. By inspecting the line plots in Fig.6.9 the vaporization characteristics are more apparent. At about $2000s$ in Fig.6.9.(a), the mass content in the domain begins to drop rapidly due to vaporization. The mass exiting the domain is represented by the jagged decrease in the mass content in Fig.6.9.(a) since the liquid phase has a higher density than the vapor phase. Figure 6.9.(b), on the other hand shows a more smooth descent to an ultimately lower liquid mass vale at the simulation end time. The temperatures at the end time for the fully vaporized case in Fig.6.9.(b) is lower than Fig.6.9.(a) since the vaporizing liquid consumes more thermal energy through latent cooling. The same observation can be made in Figs.6.7 and 6.6

The transitional points collected by testing a range of cases are presented in Fig.6.10 and identifies the flow regimes for various heat rates.

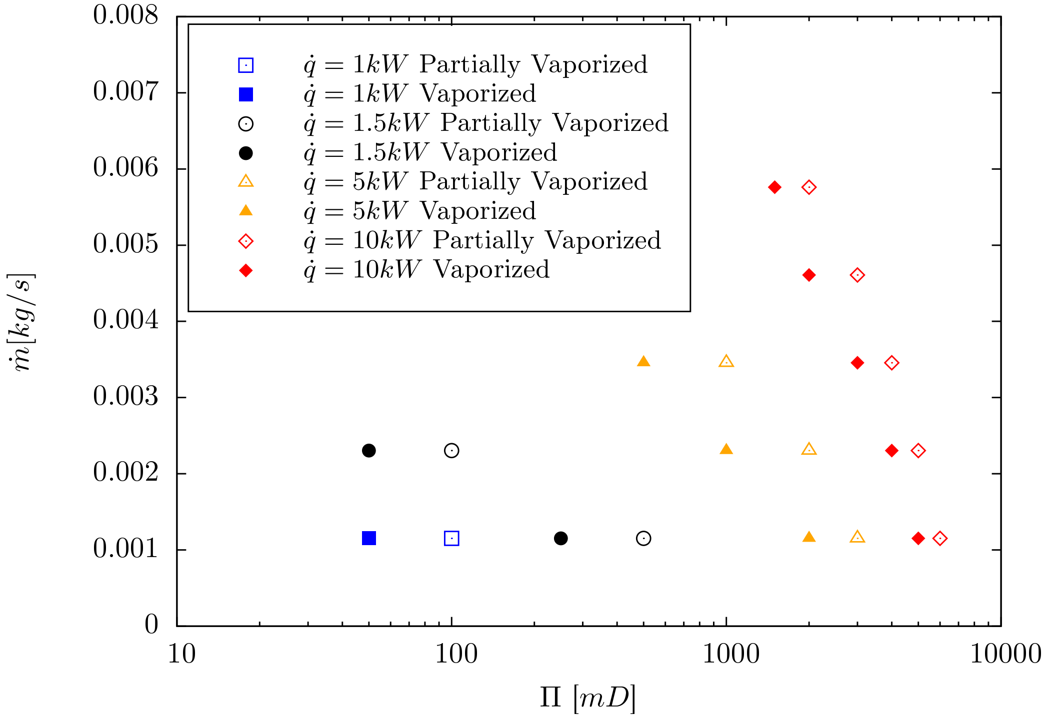

Figure 6.10: Regime map identifying the transition between full vaporization (filled shapes) and partial/incomplete vaporization (shape outline). Various shape styles/colors represent different heat rates and suggest that for higher heat rates, a wider range of flow rates and permeabilities can be utilized while achieving full vaporization.

In order to represent the data in a manner that suggests a linear relation between these parameters, the heat rate was treated as a third dimension and a surface was constructed through all of the transition loci, Fig.6.11.

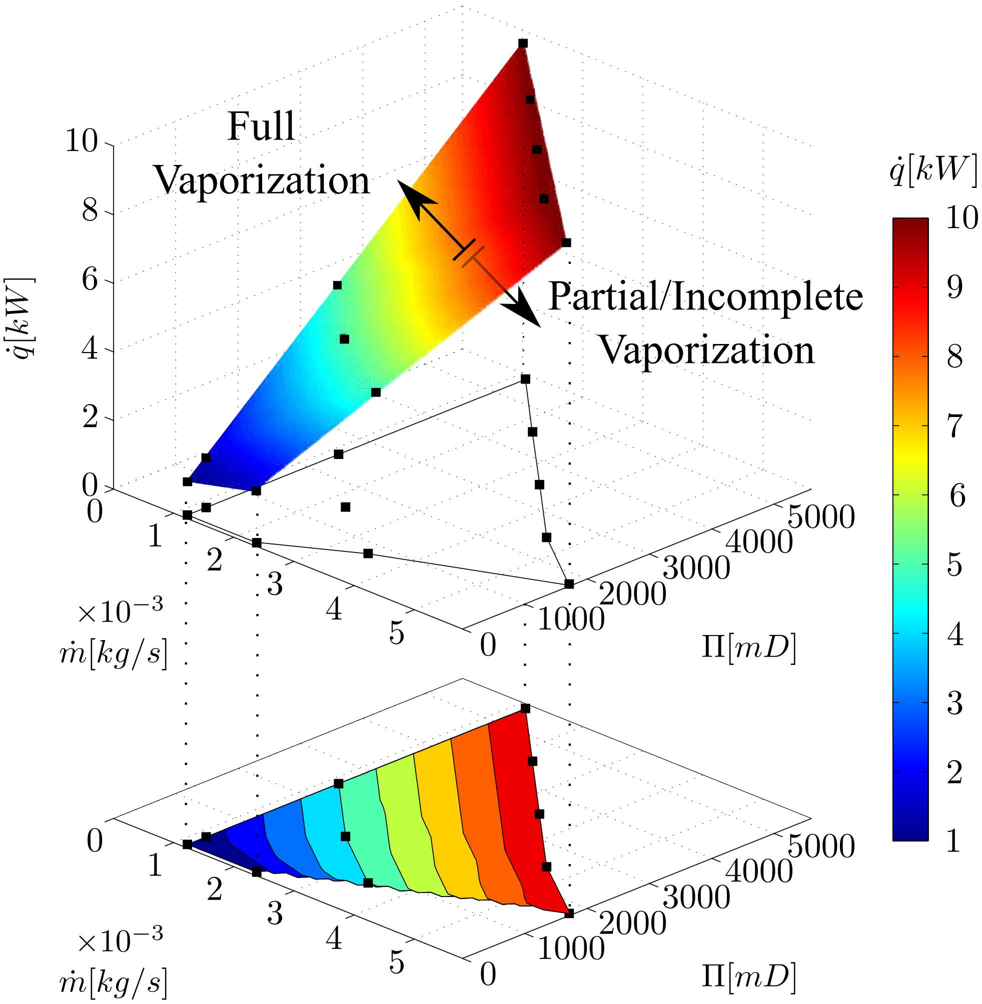

Figure 6.11: Regime map identifying the transition between full vaporization and partial/incomplete vaporization in 3D. The 3D surface outline is projected on the $\dot{q} = 0$ plane for better readability and the lower contour plot helps illustrate the near planar profile with slight curvature in the low permeability ranges. The plot suggests that that for higher heat rates, a wider range of flow rates and permeabilities can be utilized while achieving full vaporization.

Figure 6.11 provides a means for selecting a combination of heat rate and solvent delivery rate for a given permeability. It should be noted that these results are specific to a porous matrix with a porosity of $\chi = 0.32$ and for the geometric specifications provided at the beginning of this section. Any deviations from these values will result in a decrease in applicability of the data here.

6.3 Pay Zone Simulation: Gravity in Free Flow and Porous Media Regions

This section details the inclusion of gravity and the transition from free flow to porous media. Only the early transients are considered in this study as this is the time frame where the liquid/vapor interface interacts with the porous media/free flow interface. This case is the last piece of data that is necessary for tailoring the most representative case to model the phase change of liquid/vapor systems confined in porous media. It can also be useful for determining whether or not modeling the porous/free flow transition and the initial filling phase has a large impact on the vaporization of the liquid solvent. For this case, an initial free flow portion of the domain is initialized concentrically about the inlet at a diameter of $D_m = 0.483m$. An initial volume of liquid is initialized within the free flow cavity, Fig.6.12.

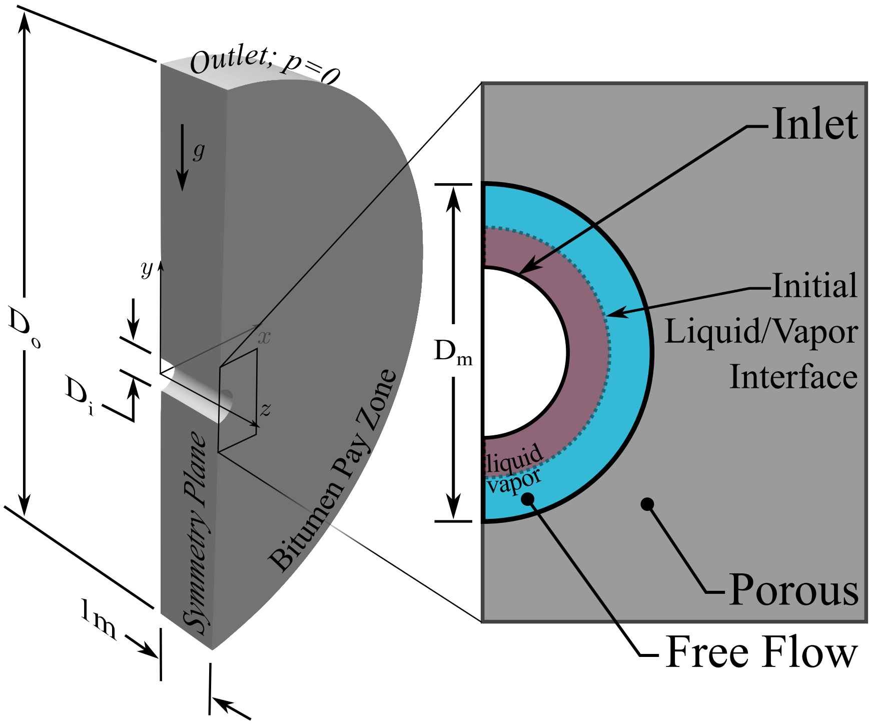

Figure 6.12: Computational domain for the case including gravity and a transition from porous media to free flowing regions.

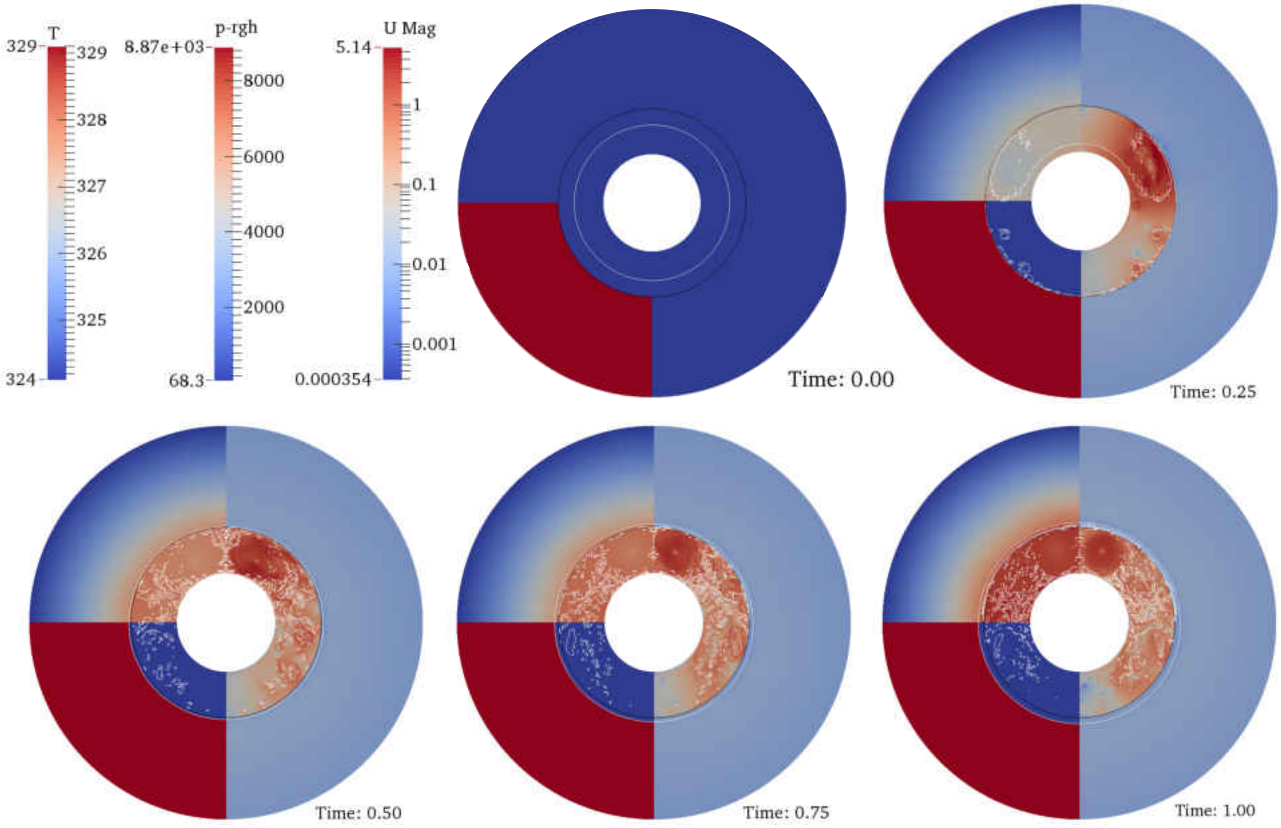

Figure 6.13: Simulation results for the case including gravity and the transition from free flow to porous media region for the first second of the simulation when the liquid/vapor interface splashes on the porous media interface. The velocity magnitude (right half of circle), pressure (upper left quadrant) and the temperature distributions (lower left quadrant) are presented at various time steps. The white and black lines are contours drawn at $\alpha = 0.5$ and $\chi = 0.32$ for the VOF field and porosity fields respectively.

The mass flow rate supplied to the domain, the permeability and porosity were selected to be $2.23kg/s$, $3 \times 10^3 mD$ and 0.32. The interface is pulled down onto the porous media/free flow interface and splashes up along the wall in the well bore. The velocity field magnitude (right hemisphere) shows the vortices forming as the fluid circulates in the free flowing portion of the domain. It is also clear that the liquid/vapor interface that penetrates the porous media has a much lower velocity when compared to the free flowing portion of the domain.

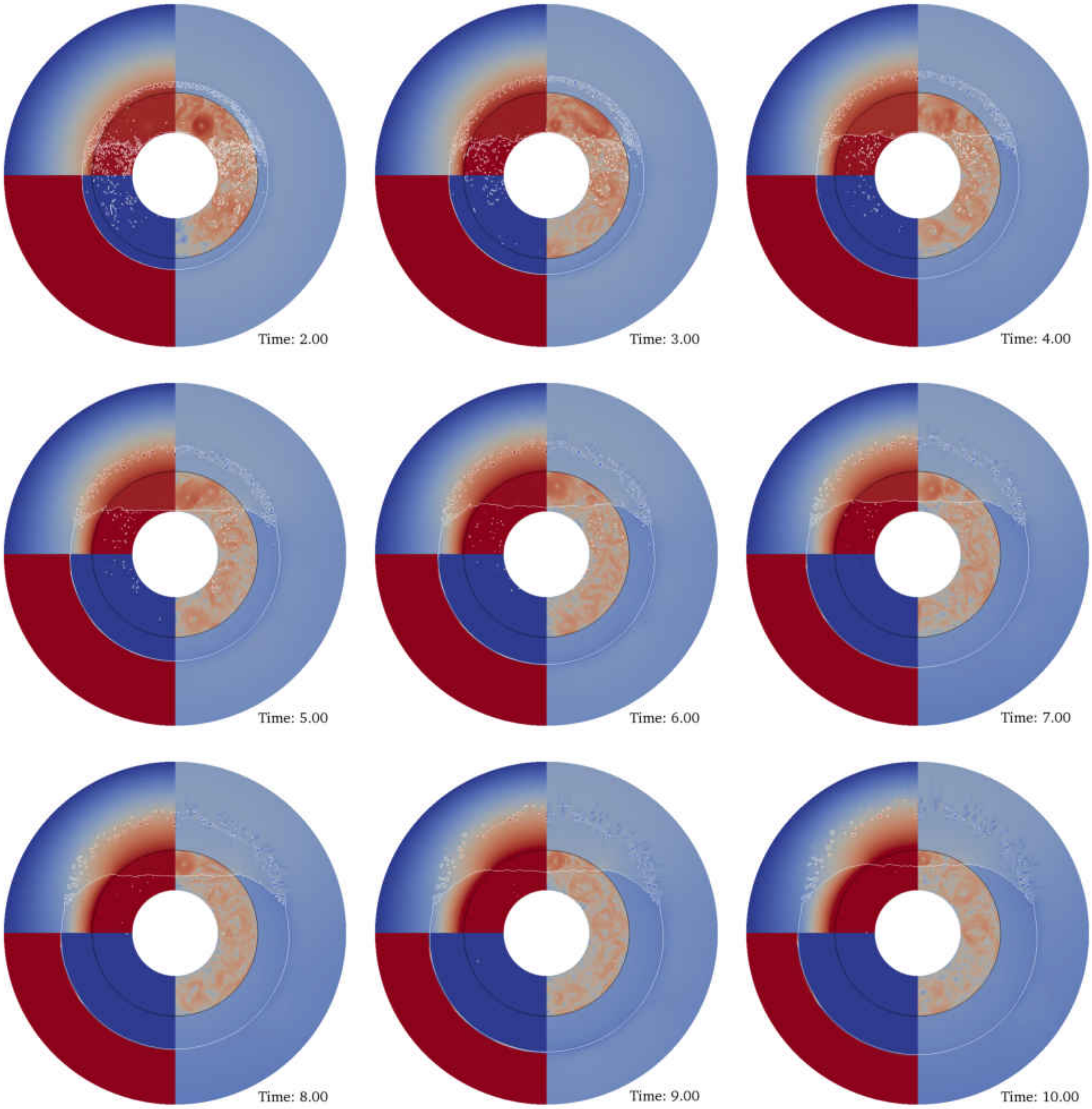

Figure 6.14: Simulation results for the case including gravity and the transition from free flow to porous media region for the remaining portion of the simulation continued from Fig.6.13 (refer to Fig.6.13 for the color map). The velocity magnitude (right half of circle), pressure (upper left quadrant) and the temperature distributions (lower left quadrant) are presented at various time steps. The white and black lines are contours drawn at $\alpha = 0.5$ and $\chi = 0.32$ for the VOF field and porosity fields respectively.

Figure 6.14 shows the remainder of the simulation as the free flow cavity fills with saturated solvent. The liquid/vapor interface that splashed on the upper wall is then forced through the porous media due to the rise in cavity pressure resulting from the addition of mass through the inlet. The temperature field in the lower left quadrant is relatively uniform in the liquid and vapor phases respectively. The onset of the heating is present; however, for the time scales considered here, the increase in temperature is minimal.

This case shows how the liquid permeates through the porous media in a manner similar to the previous case but with the addition of the free flow transition to porous media. Note that the permeability is also $3000mD$. The primary difference in the geometric configuration is the distribution of the heat source term in the energy equation. In the previous case, the liquid entering the domain passes directly into the porous media and is uniformly distributed around the inlet where the heating occurs. In this case, if the mass flow rate was identical to the previous case, the liquid would drips down onto the porous interface in the same spot at the bottom of the cavity and would carve a “thermal path” (Fig.6.8, the low temperature region where the liquid is flowing) where the temperature is closer to the saturation temperature than it is to the mean temperature. This situation would not be conducive to fully vaporizing the liquid solvent.

This additional study demonstrates the complexity of modeling near wellbore physical processes and the importance of understanding the interaction of liquid/vapor interfaces with porous structures. For all cases, the role of gravity acts to pull the liquid propane out of the heated zone and away from the injector well. In the presence of gravity, the drainage of liquid propane must either be met by high temperatures or be scaled back by reduction in flow rate in order to slow or stop the flow of liquid away from the heated zone and into the producer well. In practice, however, the infinite media away from the well decreases in pressure and as a result, the saturation temperature for the propane will inevitably decrease, resulting in full vaporization, but not necessarily in the appropriate location.

CHAPTER 7: CONCLUSION

A phase change solver was developed on the OpenFOAM platform to incorporate the effects of free flow and porous media transitions on the momentum, continuity, energy and Volume of Fluid equation. Various validations were constructed to demonstrate the robustness of the solver and its abilities to handle real and fictitious fluids in both free and porous media with precision and accuracy. The scope of the simulations presented here was to gain insight into some key concepts associated with the delivery of liquid solvent to a bitumen pay zone undergoing electromagnetic heating. The liquid solvent entering the numerical domain at the saturation temperature must be vaporized in order to effectively extract the bitumen from the pay zone. This study seeks a relation between the solvent delivery rate, heat rate and the pay zone permeability to identify the transition between full and partial/incomplete vaporization.

The pay zone simulations were decomposed into three configurations to assess the individual contributions of heating, gravity, and free flow to porous media transitions in the numerical domain. It was demonstrated that in the absence of gravity that three distinct regimes existed comprised of steady penetration of a liquid front into the heated zone, the maximum penetration depth state where the electromagnetic heating and decrease in flow speed resulting from continuity lead to the stagnation of the interface and finally, the regression of the interface due to the continued generation of heat near the injector well.

Simulations involving only porous media and gravity demonstrated that the role of gravity has a strong contribution to the vaporization of the liquid solvent. The gravitational field pulls the liquid towards the bottom of the domain and away from the heated zone, which decays away from the near wellbore region, preventing full vaporization. This decaying profile results in heat delivery rates that are many times greater than the energy required to turn the liquid solvent to vapor determined by an energy balance. Results of the parametric study from the pay zone simulations demonstrate the importance of the Darcian flow resistance forces added by the porous media to stabilize the liquid/vapor interfacial flow being pulled away from the wellbore in the presence of gravity. For all cases involving an increase in solvent delivery rate with a constant heat rate, the permeability range required for full vaporization must decrease in order to balance the gravitational forces pulling the solvent away from the heated region. For all conditions of permeability and solvent delivery rates, sufficiently increasing the heat rate results in complete vaporization of the liquid solvent. For the case of decreasing solvent delivery rate, a wider range of higher permeabilities for a given heat rate can be utilized while achieving full vaporization. A three dimensional surface outlining the transition from partially vaporized to fully vaporized regimes is constructed relating the solvent delivery rate, the permeability of the porous near wellbore zone and the heat rate supplied to the domain. For the range of permeabilities ($\approx 3000mD$) observed in these types of well bores, low solvent delivery rates and high heat rates must be utilized in order to achieve full vaporization.

APPENDIX : porousInterTempPhaseChangeFoam.C

```
/*---------------------------------------------------------------------------*\
  =========                 |
  \\      /  F ield         | OpenFOAM: The Open Source CFD Toolbox
   \\    /   O peration     |
    \\  /    A nd           | Copyright (C) 2011-2013 OpenFOAM Foundation
     \\/     M anipulation  |
-------------------------------------------------------------------------------
License
    This file is part of OpenFOAM.

    OpenFOAM is free software: you can redistribute it and/or modify it
    under the terms of the GNU General Public License as published by
    the Free Software Foundation, either version 3 of the License, or
    (at your option) any later version.

    OpenFOAM is distributed in the hope that it will be useful, but WITHOUT
    ANY WARRANTY; without even the implied warranty of MERCHANTABILITY or
    FITNESS FOR A PARTICULAR PURPOSE.  See the GNU General Public License
    for more details.

    You should have received a copy of the GNU General Public License
    along with OpenFOAM.  If not, see <http://www.gnu.org/licenses/>.

Application
    porousInterTempPhaseChangeFoam

Description
    Solver for 2 incompressible, non-isothermal immiscible fluids using a VOF
    (volume of fluid) phase-fraction based interface capturing approach.
    The momentum and other fluid properties are of the "mixture" and a single
    momentum equation is solved. Phase change is implemented by the method of
    Hardt and Wondra, 2008. Energy and momentum transfer is modeled using a
    volume averaged approach using the porosity, defined over the entire domain
    including free flowing portions.

    Turbulence modelling is generic, i.e. laminar, RAS or LES may be selected.

    For a two-fluid approach see twoPhaseEulerFoam.
```

```
    Explicit handling of porous zones is included.

\*---------------------------------------------------------------------------*/

#include "fvCFD.H"

//#include "CMULES.H"// Header which contains templates for MULES (no porosity)
//#include "porousCMULES.H"// CHANGE. This header should include porousMULES.H
        // but for some reason it doesn't.
#include "porousMULES.H"// ADD because above doesn't include it

#include "subCycle.H"
#include "interfaceProperties.H"
#include "incompressibleTwoPhaseMixture.H"
#include "turbulenceModel.H"
#include "IOporosityModelList.H"
#include "pimpleControl.H"
#include "fvIOoptionList.H"
#include "fixedFluxPressureFvPatchScalarField.H"

// * * * * * * * * * * * * * * * * * * * * * * * * * * * * * * * * * * * * * //

int main(int argc, char *argv[])
{

    #include "setRootCase.H"
    #include "createTime.H"
    #include "createMesh.H"

    #include "initContinuityErrs.H"
    #include "createFields.H"
    // Add additional fields for phase change
        #include "createFieldsPhaseChange.H"
        // Add additional fields for porous media
        #include "createFieldsPorous.H"
    #include "createPorousZones.H" //Add
    #include "readTimeControls.H"

    pimpleControl pimple(mesh);
```

```
   #include "createPrghCorrTypes.H"
   #include "correctPhi.H"
   #include "CourantNo.H"
   #include "setInitialDeltaT.H"

       // Write date
       #include "OFstream.H"
       // Write header of output data file
       #include "writeTxtHeader.H"

       // Calculate area of specified patch
       #include "calculatePatchArea.H"

// * * * * * * * * * * * * * * * * * * * * * * * * * * * * * * * * * * * //

   Info<< "\nStarting time loop\n" << endl;

   while (runTime.run())
   {
       #include "readTimeControls.H"
       #include "CourantNo.H"
       #include "porousAlphaCourantNo.H" //Modify
       #include "setDeltaT.H"

       runTime++;

       Info<< "Time = " << runTime.timeName() << nl << endl;

       // --- Pressure-velocity PIMPLE corrector loop
       while (pimple.loop())
       {
           #include "alphaControls.H"

           if (pimple.firstIter() || alphaOuterCorrectors)
           {
               twoPhaseProperties.correct();

               #include "porousAlphaEqnSubCycle.H"
```

```
        interface.correct();
    }

                // Calculate source terms for the last time step and apply them to
                // the current *TEqn.H then recalculate the source terms for the
                // updated temperature for the application in *pEqn.H
                for (int loop = 0; loop < 2; loop++)
                {
                        #include "calculateSourceTerms.H"
                if (loop == 0)
                {
                                #include "porousTEqn.H"
                }
            }

    #include "porousUEqn.H"

    // --- Pressure corrector loop
    while (pimple.correct())
    {
        #include "porousPEqn.H"
    }

    if (pimple.turbCorr())
    {
        turbulence->correct();
    }
}

        // Monitor mass conservation
        #include "calculatePatchMassFlux.H"
        // Calculate Nusselt number along specified patch
        #include "calculateMeanNusseltNumber.H"

        if (runTime.outputTime())
        {
                // Write data for post processing
                #include "infoOutput.H"
        }
```

```
        runTime.write();

        Info<< "ExecutionTime = " << runTime.elapsedCpuTime() << " s"
            << "  ClockTime = " << runTime.elapsedClockTime() << " s"
            << nl << endl;
    }

    Info << "End\n" << endl;

    return 0;
}


// ************************************************************************* //
```

REFERENCES

[1] Stephen Rassenfoss et al. Oil sands get wired-seeking more oil, fewer emissions. *Journal of Petroleum Technology*, 64(09):34–45, 2012.

[2] Albina Mukhametshina and Elena Martynova. Electromagnetic heating of heavy oil and bitumen: A review of experimental studies and field applications. *Journal of Petroleum Engineering*, 2013, 2013.

[3] RA Wooding. Steady state free thermal convection of liquid in a saturated permeable medium. *Journal of Fluid Mechanics*, 2(03):273–285, 1957.

[4] HC Brinkman. On the permeability of media consisting of closely packed porous particles. *Applied Scientific Research*, 1(1):81–86, 1949.

[5] CT Hsu and P Cheng. Thermal dispersion in a porous medium. *International Journal of Heat and Mass Transfer*, 33(8):1587–1597, 1990.

[6] S Hardt and F Wondra. Evaporation model for interfacial flows based on a continuum-field representation of the source terms. *Journal of Computational Physics*, 227(11):5871–5895, 2008.

[7] Christian Kunkelmann. Numerical modeling and investigation of boiling phenomena. 2011.

[8] Stephen Whitaker. Simultaneous heat, mass, and momentum transfer in porous media: a theory of drying. 1977.

[9] Ping Cheng. Heat transfer in geothermal systems. *Advances in heat transfer*, 14:1–105, 1978.

[10] Roger Young. Two-phase brine mixtures in the geothermal context and the polymer flood model. *Transport in porous media*, 11(2):179–185, 1993.

[11] DA Pruzan, KE Torrance, and CT Avedisian. Two-phase flow and dryout in a screen wick saturated with a fluid mixture. *International journal of heat and mass transfer*, 33(4):673–681, 1990.

[12] Linda M Abriola. Multiphase flow and transport models for organic chemicals: A review and assessment: Final report. Technical report, Electric Power Research Inst., Palo Alto, CA (USA); Michigan Univ., Ann Arbor (USA). Dept. of Civil Engineering, 1988.

[13] JC Parker. Multiphase flow and transport in porous media. *Reviews of Geophysics*, 27(3):311–328, 1989.

[14] Jacques Burger, Pierre Sourieau, and Michel Combarnous. Thermal methods of oil recovery. 1986.

[15] CY Wang and P Cheng. A multiphase mixture model for multiphase, multicomponent transport in capillary porous mediai. model development. *International journal of heat and mass transfer*, 39(17):3607–3618, 1996.

[16] PS Huyakorn, S Panday, and YS Wu. A three-dimensional multiphase flow model for assesing napl contamination in porous and fractured media, 1. formulation. *Journal of Contaminant Hydrology*, 16(2):109–130, 1994.

[17] Jacob Bear. *Dynamics of fluids in porous media*. Courier Corporation, 2013.

[18] S Abaci, JS Edwards, and BN Whittaker. Relative permeability measurements for two phase flow in unconsolidated sands. *Mine water and the environment*, 11(2):11–26, 1992.

[19] Mohammed F Karim, Katsutoshi Tanimoto, Phung D Hieu, et al. Simulation of wave transformation in vertical permeable structure. *International Journal of Offshore and Polar Engineering*, 14(02), 2004.

[20] Bruno AM Carciofi, Marc Prat, and Joao B Laurindo. Homogeneous volume-of-fluid (vof) model for simulating the imbibition in porous media saturated by gas. *Energy & Fuels*, 25(5):2267–2273, 2011.

[21] Ching-Yao Chen, Yu-Sheng Huang, and José A Miranda. Radial hele-shaw flow with suction: Fully nonlinear pattern formation. *Physical Review E*, 89(5):053006, 2014.

[22] Behnam Ebrahimi, Seyed-Mohammad Taghavi, and Kayvan Sadeghy. Two-phase viscous fingering of immiscible thixotropic fluids: A numerical study. *Journal of Non-Newtonian Fluid Mechanics*, 218:40–52, 2015.

[23] Mark Sussman and Elbridge Gerry Puckett. A coupled level set and volume-of-fluid method for computing 3d and axisymmetric incompressible two-phase flows. *Journal of Computational Physics*, 162(2):301–337, 2000.

[24] J López and J Hernández. Analytical and geometrical tools for 3d volume of fluid methods in general grids. *Journal of Computational Physics*, 227(12):5939–5948, 2008.

[25] Petar Liovic, Murray Rudman, Jong-Leng Liow, Djamel Lakehal, and Doug Kothe. A 3d unsplit-advection volume tracking algorithm with planarity-preserving interface reconstruction. *Computers & fluids*, 35(10):1011–1032, 2006.

[26] Jure Mencinger and Iztok Žun. A plic–vof method suited for adaptive moving grids. *Journal of Computational Physics*, 230(3):644–663, 2011.

[27] G Son and VK Dhir. Numerical simulation of film boiling near critical pressures with a level set method. *Journal of Heat Transfer*, 120(1):183–192, 1998.

[28] Gihun Son and Vijay K Dhir. A level set method for analysis of film boiling on an immersed solid surface. *Numerical Heat Transfer, Part B: Fundamentals*, 52(2):153–177, 2007.

[29] Frédéric Gibou, Liguo Chen, Duc Nguyen, and Sanjoy Banerjee. A level set based sharp interface method for the multiphase incompressible navier–stokes equations with phase change. *Journal of Computational Physics*, 222(2):536–555, 2007.

[30] SP Zhang, MJ Ni, and HY Ma. Vof method for simulation of multiphase incompressible flows with phase change. In *RECENT PROGRESSES IN FLUID DYNAMICS RESEARCH: Proceeding of the Sixth International Conference on Fluid Mechanics*, volume 1376, pages 579–581. AIP Publishing, 2011.

[31] Christian Kunkelmann and Peter Stephan. Modification and extension of a standard volume-of-fluid solver for simulating boiling heat transfer. In *Proc. 5th European Conference on Computational Fluid Dynamics ECCOMAS CFD2010, Lisbon, Portugal*, 2010.

[32] Christian Kunkelmann and Peter Stephan. Cfd simulation of boiling flows using the volume-of-fluid method within openfoam. *Numerical Heat Transfer, Part A: Applications*, 56(8):631–646, 2009.

[33] Christian Kunkelmann and Peter Stephan. Numerical simulation of the transient heat transfer during nucleate boiling of refrigerant hfe-7100. *International Journal of refrigeration*, 33(7):1221–1228, 2010.

[34] G Tomar, G Biswas, A Sharma, and A Agrawal. Numerical simulation of bubble growth in film boiling using a coupled level-set and volume-of-fluid method. *Physics of Fluids (1994-present)*, 17(11):112103, 2005.

[35] BM Ningegowda and B Premachandran. A coupled level set and volume of fluid method for phase change problems.

[36] Qingyun Zeng, Jiejin Cai, Huaqiang Yin, Xingtuan Yang, and Tadashi Watanabe. Numerical simulation of single bubble condensation in subcooled flow using openfoam. *Progress in Nuclear Energy*, 83:336–346, 2015.

[37] Damir Juric and Grétar Tryggvason. Computations of boiling flows. *International Journal of Multiphase Flow*, 24(3):387–410, 1998.

[38] Ichiro Tanasawa. Advances in condensation heat transfer. *Advances in heat transfer*, 21:55–139, 1991.

[39] Asghar Esmaeeli and Grétar Tryggvason. Computations of film boiling. part ii: multi-mode film boiling. *International journal of heat and mass transfer*, 47(25):5463–5476, 2004.

[40] C Beckermann and R Viskanta. Natural convection solid/liquid phase change in porous media. *International journal of heat and mass transfer*, 31(1):35–46, 1988.

[41] Gaurav Tomar. Two-phase flow with phase change in porous channels. *Journal of Thermal Science and Engineering Applications*, 7(2):021006, 2015.

[42] Yanis C Yortsos and Athanassios K Stubos. Phase change in porous media. *Current opinion in colloid & interface science*, 6(3):208–216, 2001.

[43] Michael Le Bars and M Worster. Interfacial conditions between a pure fluid and a porous medium: implications for binary alloy solidification. *Journal of Fluid Mechanics*, 550:149–173, 2006.

[44] H Weller. A new approach to vof-based interface capturing methods for incompressible and compressible flow, opencfd ltd. Technical report, Report TR/HGW/04, 2008.

[45] Steven T Zalesak. Fully multidimensional flux-corrected transport algorithms for fluids. *Journal of computational physics*, 31(3):335–362, 1979.

[46] Henrik Rusche. *Computational fluid dynamics of dispersed two-phase flows at high phase fractions*. PhD thesis, Imperial College London (University of London), 2003.

[47] Samuel WJ Welch and John Wilson. A volume of fluid based method for fluid flows with phase change. *Journal of computational physics*, 160(2):662–682, 2000.

[48] BA Younglove and James F Ely. Thermophysical properties of fluids. ii. methane, ethane, propane, isobutane, and normal butane. *Journal of Physical and Chemical Reference Data*, 16(4):577–798, 1987.

[49] PJ Berenson. Film-boiling heat transfer from a horizontal surface. *Journal of Heat Transfer*, 83(3):351–356, 1961.

[50] Vivek Peraser, Shirish Liladhar Patil, Santanu Khataniar, Abhijit Yeshwant Dandekar, Vikas S Sonwalkar, et al. Evaluation of electromagnetic heating for heavy oil recovery from alaskan reservoirs. In *SPE Western Regional Meeting*. Society of Petroleum Engineers, 2012.